ABSTRACT

Title of dissertation: COMPLEX FLOWS IN GRANULAR
                           AND QUANTUM SYSTEMS

                           Mark Richard Herrera
                           Doctor of Philosophy, 2013

Dissertation directed by: Professor Edward Ott
                           Department of Physics

In this thesis we investigate three problems involving complex flows in granular and quantum systems.

(a) We first study the dynamics of granular particles in a split-bottom shear cell experiment. We utilize network theory to quantify the dynamics of the granular system at the mesoscopic scale. We find an apparent phase transition in the formation of a giant component of broken links as a function of applied shear. These results are compared to a numerical model where breakages are based on the amount of local stretching in the granular pile.

(b) Moving to quantum mechanical systems, we study revival and echo phenomena in systems of anharmonically confined atoms, and find a novel phenomena we call the "pre-revival echo". We study the effect of size and symmetry of the perturbations on the various echoes and revivals, and form a perturbative model to describe the phenomena. We then model the effect of interactions using the Gross-Pitaevskii Equation and study interactions' effect on the revivals.

(c) Lastly, we continue to study the effect of interactions on particles in weakly anharmonic traps. We numerically observe a "dynamical localization" phenomena in the presence of both anharmonicity and interactions. States may remain localized or become spread out in the potential depending on the strength and sign of the anharmonicity and interactions. We formulate a model for this phenomena in terms of a classical phase space.

COMPLEX FLOWS IN GRANULAR
AND QUANTUM SYSTEMS

by

Mark Richard Herrera

Dissertation submitted to the Faculty of the Graduate School of the
University of Maryland, College Park in partial fulfillment
of the requirements for the degree of
Doctor of Philosophy
2013

Advisory Committee:
Professor Edward Ott, Chair/Advisor
Professor Thomas M. Antonsen, Co-Advisor
Professor Michelle Girvan
Professor Wolfgang Losert
Professor Thomas Murphy

Preface

The work in this thesis includes the following publications/preprints:

- The path to fracture: dynamics of broken-link networks in granular flows

  M. Herrera, S. McCarthy, S. Slotterback, E. Cephas, W. Losert, and M. Girvan, Phys. Rev. E 83, 061303 (2011)

- Echoes and revival echoes in systems of anharmonically confined atoms

  M. Herrera, T.M. Antonsen, E. Ott, and S. Fishman, Phys. Rev. A 86, 023613 (2012)

- Dynamic localization of a weakly interacting Bose-Einstein condensate in an anharmonic potential

  M. Herrera, T.M. Antonsen, E. Ott, and S. Fishman, Phys. Rev. A 87, 041603(R) (2013)

Dedication

To my wife, Camille.

Acknowledgments

First, I thank my co-advisors, Prof. Edward Ott and Prof. Thomas Antonsen for giving me the opportunity to work on interesting projects over the past three years. This thesis would not be possible without their patient guidance, as well as their extraordinary theoretical ideas and computational expertise. Additionally, I thank Prof. Wolfgang Losert and Prof. Michelle Girvan for their scientific expertise and guidance on the granular component of my thesis, as well as throughout my graduate career. Thank you also to Prof. Tom Murphy for taking the time to be a member of my thesis committee.

I owe special thanks to Prof. Shmuel Fishman of Technion-Israel Institute of Technology, for not only guiding me as a collaborator, but also hosting me in Israel and helping to make this thesis a reality. Thanks also to his students: Yevgeny Kripolov, Hagar Veksler, Alexandra Bachman, and Erez Michaely for their useful scientific input and for being excellent hosts.

Further thanks are owed to Prof. Steve Rolston for providing insight into experimental systems and helping me find regimes where theory is subject to empirical testing. Thanks also to Dr. John Palastro who has been invaluable in providing support in writing this thesis.

Special thanks are also in order to the scientists in the granular laboratory: Steve Slotterback, Matthew Harrington, Kerstin Nordstrom, and Mitch Mailman. This thesis is a direct result of their excellent advising and collaboration.

Thanks are also in order to the other graduate students in the nonlinear dy-

Table of Contents

List of Figures

List of Abbreviations

IREAP	Institute for Research in Electronics and Applied Physics
NSF	National Science Foundation
DoD	Department of Defense
NDSEG	National Defense Science and Engineering Graduate Fellowship
BSF	Binational Science Foundation
BEC	Bose Einstein Condensate
GPE	Gross-Pitaevskii Equation
FFT	Fast Fourier Transform
QED	Quantum Electrodynamics

Chapter 1

Introduction

This thesis can be broadly broken down into two parts:

1. Network theoretic approaches to describe granular flows.

2. The dynamics of cold atoms in quasi-1D potentials.

1.1 Complex Networks and Granular Systems

Complex network science is a relatively new field found at the intersection of mathematics, physics, biology, and informatics. A thorough review of network science is given in Ref. [1], with applications to a variety of fields. A network is a collection of objects called nodes (or vertices) which are connected via edges (or links). These nodes and edges can represent different objects or concepts depending on the particular application. For example, in the context of gene regulatory networks, genes are represented by nodes, and edges are included between genes if there is some causal relationship between the states of the genes. Other examples include networks of scientific keywords [2], where edges represent papers in which keywords appear together, coauthorship networks [3–5], intermarriages between families [6], and epidemiological models of disease spread [7]. Many more examples of networks can be found in [1].

This thesis will be concerned, in part, with the study of granular flows through

the lens of network theory. Granular materials consist of a large ensemble of solid particles that interact through contact and dissipative forces. A thorough review of granular material is given in [8]. Moreoever, the grains are large enough that they do not experience motion due thermal fluctuations. Granular materials can exhibit properties of various states of matter depending on their preparation and strain. For example, a sand dune can maintain its shape when a load is placed upon it, but sand can also be made to flow as a liquid, such as in an hourglass. Earlier theoretical work in the dynamics of granular materials applied a continuum model to these systems, for example, the Mohr-Columomb theory applied to find the thickness of the shear zone [9].

Forces in dense granular materials are transmitted through an intricate network of particle contacts. In jammed granular matter, this contact network is able to support stresses and strains up to a yield stress. However, under large enough stress or strain, the material will yield and deform, as particle contacts fail. This failure of the jammed state gives way to flow. The reproducible nature of many flow fields [10, 11] of granular matter indicates that the particle contacts fail as a continuum. However, it is not possible to fully leave the particle scale: shear band widths can be as small as five particle diameters, so unlike in solid mechanics or fluid dynamics, the scale of gradients in velocity is not well separated from the particle scale. Therefore continuum equations, for example, the velocity field cannot be fully justified.

In this thesis, we propose the application of network theory to study the intermediate, meso-scale features to describe granular flows. Network theory, concerned

with the collective interaction of subsets of nodes, is a uniquely suitable tool to study these dense flows. We will find that this approach provides a characteristic strain scale on which fracture in the dense pile occurs.

1.2 Bose Einstein Condensation and the Gross-Pitaevskii Equation

First experimentally observed in 1995 [12–14], a Bose-Einstein condensate is a dilute collection of atoms where are a macroscopic fraction of atoms are in the same quantum state $\psi(\boldsymbol{r})$. Here we follow the derivation of Pethick and Smith [15] for the equations of motion for this quantum state using a mean field approach at zero temperature. Other derivations using second-quantization have also been applied, for example see Refs. [16, 17].

At low energies, the interaction between two particles at low energies is a constant in the momentum representation $U_0 = 4\pi\hbar^2 a/m$, where a, the s-wave scattering length [15]. In the position representation, the interaction is a contact potential

$$U_{int} = U_0\delta(\boldsymbol{r} - \boldsymbol{r'}). \tag{1.1}$$

Consider a collection of N atoms in a trapping potential $V(\boldsymbol{r})$. Using a Hartree or mean-field approach, we assume the N-body wave function is a symmetrized product of single-particle wave functions:

$$\Psi(\boldsymbol{r_1}, \boldsymbol{r_2}, \ldots, \boldsymbol{r_N}) = \prod_{i=1}^{N} \phi(\boldsymbol{r_1}). \tag{1.2}$$

The Hamlitonian for this system is given as the sum of the individual kinetic and

potential energies for each atom, plus the sum over all pairs of interacting particles:

$$H = \sum_{i=1}^{N} \left[\frac{p_i^2}{2m} + V(r_i) \right] + U_0 \sum_{i<j} \delta(\mathbf{r_i} - \mathbf{r_j}) \tag{1.3}$$

The energy of the total system is then

$$E = N \int d\boldsymbol{r} \left[\frac{\hbar^2}{2m} |\nabla \phi(\boldsymbol{r})|^2 + V(r)|\phi(\boldsymbol{r})|^2 + \frac{(N-1)}{2} U_0 |\phi(\boldsymbol{r})|^4 \right]. \tag{1.4}$$

For convenience, it is useful to define a scaled condensate wavefunction, $\psi(\boldsymbol{r}) = \sqrt{N}\phi(\boldsymbol{r})$. Dropping terms of order $1/N$, the energy of the system can then be written as

$$E(\psi) = \int d\boldsymbol{r} \left[\frac{\hbar^2}{2m} |\nabla \psi(\boldsymbol{r})|^2 + V(r)|\psi(\boldsymbol{r})|^2 + \frac{1}{2} U_0 |\psi(\boldsymbol{r})|^4 \right]. \tag{1.5}$$

In order to find the optimal conditions for ψ, one can apply a calculus of variations approach to minimize $E(\psi)$ with respect to ψ and ψ^*. Constraining the total number of particles

$$N = \int d\mathbf{r} |\psi(\mathbf{r})|^{\mathbf{2}} \tag{1.6}$$

to be constant, we introduce a Lagrange multiplier μ to account for this constraint. The functional to be minimized is then $E - \mu N$, for fixed μ. Calculating the variation of $E - \mu N$ with respect to ψ^*, and setting it equal to zero, $\delta E - \mu \delta N = 0$, yields the time independent Gross-Pitaevskii equation:

$$-\frac{\hbar^2}{2m} \nabla^2 \psi(\boldsymbol{r}) + V(\boldsymbol{r})\psi(\boldsymbol{r}) + U_0 |\psi(\boldsymbol{r})|^2 \psi(\boldsymbol{r}) = \mu \psi(\boldsymbol{r}). \tag{1.7}$$

Note that this expression has the same form as the usual Schrödinger equation except that it contains a nonlinear term $\sim |\psi|^2 \psi$. The nonlinear eigenvalue μ is

the chemical potential, not the energy per particle as it usually is in the linear Schrödinger equation.

In order to treat dynamical problems, it is natural to use a time-dependent generalization of the Schrödinger equation with the same nonlinear-interaction term.

$$i\hbar\frac{\partial}{\partial t}\psi(\boldsymbol{r}) = -\frac{\hbar^2}{2m}\nabla^2\psi(\boldsymbol{r}) + V(\boldsymbol{r})\psi(\boldsymbol{r}) + U_0|\psi(\boldsymbol{r})|^2\psi(\boldsymbol{r}) \tag{1.8}$$

In order to derive the time-dependent Gross-Pitaevskii equation, a variational approach analogous to the one above for the time-independent problem is useful. Eq. (1.8) can be derived by the action principal:

$$\delta S = 0 \tag{1.9}$$

$$S = \int_{t_1}^{t_2} L dt \tag{1.10}$$

$$L = \int d\boldsymbol{r}\frac{i\hbar}{2}\left(\psi^*\frac{\partial\psi}{\partial t} - \psi\frac{\partial\psi^*}{\partial t}\right) - E \tag{1.11}$$

where E is the energy given in Eq. (1.5). Applying a variational principal approach to minimize the action leads to Eq. (1.8). The time-dependent Gross-Pitaevskii equation has also been derived by treating ψ as second quantized operators, deriving the Heisenberg equations of motion, and then replacing the quantum mechanical operators with a classical field, for example in [15, 18].

1.2.1 The GP Equation in Quasi-1D Systems

In Chapters 3 and 4 of the thesis, we study the behavior of BECs confined to highly anisotroptic, quasi-1D traps. This situation is a commonly studied problem, for example in [17, 19, 20], and we follow the derivation presented in [21].

Again starting with Eq. (1.8), we consider a highly asymmetric trapping potential,

$$V(\boldsymbol{r}) = \frac{1}{2}m\omega_\perp^2(s^2) + V(z) \qquad (1.12)$$

where $s = \sqrt{x^2 + y^2}$. For a highly asymmetric "cigar" trap, the confinement is the transverse direction is much tighter than in the axial direction. Assuming the energy splitting in the transverse direction is much higher than the nonlinear interaction energy per atom, the transverse component of the wavefunction is given by the ground-state of the harmonic oscillator, and the wave function can be factored as:

$$\psi(\boldsymbol{r}) = \frac{1}{\sqrt{\pi}a_\perp}\exp\left(-\frac{s^2}{a_\perp^2}\right)\tilde{\psi}(z,t). \qquad (1.13)$$

Taking the expression for $\psi(\boldsymbol{r})$, substituting into Eq. (1.8), and integrating of the transverse direction leads to the quasi-1D, time dependent GP equation:

$$i\hbar\frac{\partial\tilde{\psi}}{\partial t} = \left(-\frac{\hbar^2}{2m}\frac{\partial^2}{\partial z^2} + V(z) + g_{1D}|\tilde{\psi}|^2\right)\tilde{\psi} \qquad (1.14)$$

where $g_{1D} = 2a_s\hbar\omega_\perp$. In Chapters 3 and 4, we work with the unitless GP Eqn. (see Appendix A).

1.3   Outline of Thesis

In Chapter 2 we study the dynamics of granular particles in a split-bottom shear cell experiment. We utilize network theory to quantify the dynamics of the granular system and the mesoscopic scale. We find an apparent phase transition in the formation of a giant component of broken links as a function of applied shear.

These results are compared to a numerical model where breakages are based on the amount of local stretching in the granular pile.

Moving to quantum mechanical systems, in Chapter 3, we study revival and echo phenomena in systems of anharmonically confined atoms, and find a novel phenomena we call the "pre-revival echo." We study the effect of size and symmetry of the perturbations on the various echoes and revivals, and form a perturbative model to describe the pheomena. We then model the effect of interactions using the Gross-Pitaevskii equation and study interactions' effect on the revivals.

Lastly, in Chapter 4, we continue to study the effect of interactions on particles in weakly anharmonic traps. We numerically observe a "dynamical localization" phenomena in the presence of both anharmonicity and interactions. States may remain localized or become spread out in the potential depending on the strength and sign of the anharmonicity and interactions. We formulate a model for this phenomena in terms of a classical phase space.

Miscellaneous information regarding normalization conventions, Wigner and Husimi representations, and numerical methods are contained in the various Appendices.

Chapter 2

The Path to Fracture in Granular Flows: Dynamics of Contact

Networks

This chapter is based on work contained in the publication: The path to fracture: dynamics of broken-link networks in granular flows, M. Herrera, S. McCarthy, S. Slotterback, E. Cephas, W. Losert, and M. Girvan, Phys. Rev. E 83, 061303 (2011), ©2011 by the American Physical Society. The experiments in this chapter where carried out by S. Slotterback.

2.1   Abstract

Capturing the dynamics of granular flows at intermediate length scales can often be difficult. We propose studying the dynamics of contact networks as a new tool to study fracture at intermediate scales. Using experimental 3D flow fields with particle scale resolution, we calculate the time evolving broken-links network and find that a giant component of this network is formed as shear is applied to this system. We implement a model of link breakages where the probability of a link breaking is proportional to the average rate of longitudinal strain (elongation) in the direction of the edge and find that the model demonstrates qualitative agreement with the data when studying the onset of the giant component. We note, however, that the broken-links network formed in the model is less clustered than our empir-

ical observations, indicating that the model reflects less localized breakage events and does not fully capture the dynamics of the granular flow.

2.2   Introduction

Forces in dense granular materials are transmitted through an intricate network of particle contacts. In jammed granular matter, this contact network is able to support stresses and strains up to a yield stress. However, under large enough stress or strain, the material will yield and deform, as particle contacts fail. This failure of the jammed state gives way to flow. The reproducible nature of many flow fields [10, 11] of granular matter indicates that the particle contacts fail as a continuum. However, it is not possible to fully leave the particle scale: shear band widths can be as small as five particle diameters, so unlike in solid mechanics or fluid dynamics, the scale of gradients in velocity is not well separated from the particle scale. Therefore continuum equations, for example the velocity field, cannot be fully justified.

The dynamics of dense granular materials are also not amenable to a purely single particle view. Indeed, the physics of force networks as well as dynamics near jamming highlight the importance of the intermediate scale. However, actually measuring this intermediate scale is challenging: under shear strain, force correlations can be found for particles more than 10 particle diameters apart [22], and cooperative structures such as force loops [23] have been found. The force correlations in the direction of the principal stress axis approximately follow a power law. String-

like dynamics in which strings of particles are observed to move cooperatively do not exhibit a preferred length scale but rather a wide, power-law like distribution of lengths [24]. Elucidating collective dynamics in flows is further complicated since string-like dynamics are defined relative to a random fluctuating background, not relative to an overall flow.

This intermediate scale is however ideal for observation through the lens of network theory, and we propose to utilize such an approach to study the onset of fracture in 3D structure. The heavy-tailed characteristics of both forces and string-like dynamics suggests no characteristic length scale exists. Instead of attempting to discover a characteristic length scale, our analysis produces the characteristic deformation of the whole system over which the contact network is substantially altered.

Surprisingly little is known about the arrangement of grain contacts in a 3D jammed state in experiments, since grains are not transparent to standard imaging methods. Numerous studies have characterized the force network at the boundaries of 3D packings, for example Mueth et. al. used carbon paper to measure forces on the boundary of a cylindrical cell filled with glass beads and subjected to uniaxial compression [25]. Techniques for obtaining the interior contact network include freezing the arrangement with glue and cutting slices through the material or layer-by-layer removal of the grains, but these are destructive methods and are not suitable for investigations of system dynamics.

Very recently, complex network methods have been used to analyze the computationally derived force network present in a granular material [26–28]. The focus

of these studies is on the characterization of the instantaneous contacts and forces in the system. In this chapter we introduce the time-evolving broken-links network as a new way to characterize particle rearrangement events in our experimental 3D granular flow. We utilize the language of percolation on networks to describe the dynamics of the network [29, 30]. This approach provides interesting results on the intermediate length and time scales that are difficult to capture with continuum or particle based approaches. The application of network theoretic concepts to this broken link network provides new insights at this intermediate length (and time) scale. Additionally, we implement a model of fracture based on the average rate of longitudinal strain and compare its results to our experimental data.

2.3 3D Shear Flows: Imaging and Processing

We determine the three dimensional microstructure of a jammed granular material using a laser sheet scanning approach we have described previously [31] which was adapted to study granular shear flows. The split-cell geometry as described in [32] consists of a $(15\text{cm})^3$ cell with a 9cm diameter disk embedded in the bottom. The cell contains 5mm diameter acrylic beads immersed in an index matched triton and laser dye (Nile Blue 690 Perchlorate) solution, and is filled to a height of 10 particle diameters. The experiment is schematized in Figure 2.1a. Figure 2.1b displays an example of an illuminated cross section of the granular flow. We shear the system at a constant rate $\Omega = 1.05 \times 10^{-3}$ rad/s, pausing in three degree increments to recover the proximity network as a function of shear (and therefore
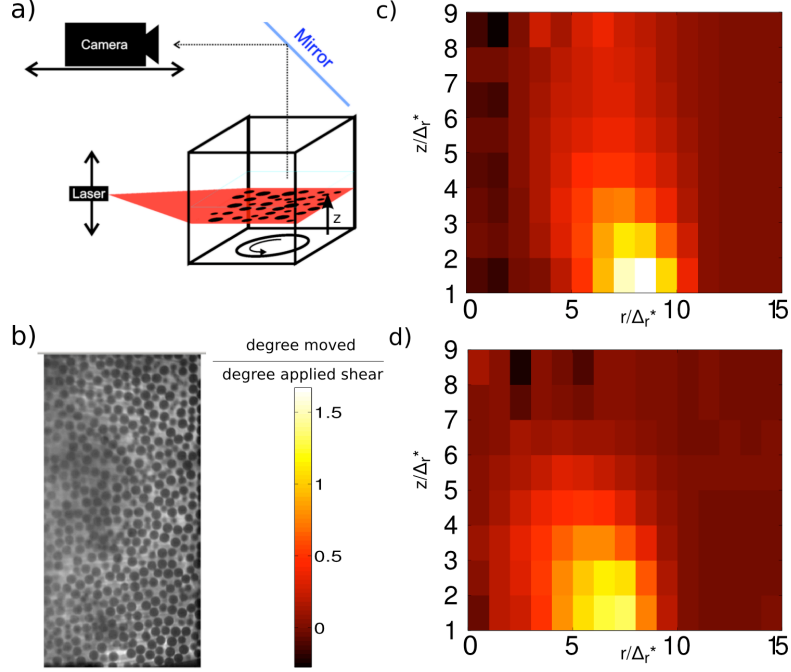
Figure 2.1: (a) Schematic of our experimental setup, a 3D granular imaging method using a laser sheet to illuminate cross sections of the index matched, laser dyed shear cell fluid. (b) An example of an illuminated cross section of the granular flow. (c) $\frac{1}{\Omega} r \frac{\partial \omega}{\partial r}$ and (d) $\frac{1}{\Omega} r \frac{\partial \omega}{\partial z}$ the r and z components of the numeric angular velocity gradient. The region of large gradients corresponds to an area close to the disk edge. Distances are normalized by the particle contact cutoff $\Delta_r^* = 24.5$ (see Figure 2.2).

time). By scanning a laser, we are able to image slightly more than half the shear cell and reconstruct the individual particle positions in 3D as a function of time. We bin particle velocities in both r (the radial distance from the center of the disk in cylindrical coordinates) and z (the height above the disk) and compute the average angular velocity ω, and its derivatives with respect to r and z shown in Figures 2.1c and 2.1d. These quantities are used to develop a simple model for link breakage

events due to longitudinal strain. The precision of the particle positions in the shear cell is approximately 2% of the radial cutoff defined below.

In order to recover a network linking proximate particles, we need to define which particles interact as neighbors. However, it is not possible to detect with certainty whether particle pairs are touching - even a nm scale gap between particles would suffice to prevent force transmission between particles. Therefore we investigate, as a dynamic, statistical metric of neighbor interactions, how particles move with respect to nearby neighbors. Recent work [33–35] has demonstrated that under small forcing, particles in a jammed system predominantly roll or slide past neighbors. The distribution in the angle, α, between the relative displacement vector of a pair of particles and the vector connecting their particle centers is peaked for tangential displacements, indicative of sliding or rolling behavior. For an ensemble of pairs of particles that do not touch and move independently the distribution is uniform, independent of $\cos(\alpha)$ (for dynamics in three dimensions, for 2D motion it would be independent of α). Thus, by varying the threshold of radial displacements between particles and observing the distribution of the α cosines, $P[\cos(\alpha)]$, we can determine an upper bound for particle contact. Figure 2.2 plots the peak value of the distribution of $\cos(\alpha)$ vs. radial displacements. We note that there is a steep decline in the peak value of the distribution (and hence an increasing flatness in the distribution) for increasing radial displacement. By selecting the displacement immediately preceding the steep decline, we conservatively select a maximum threshold for particle contact. All particle pairs closer than the specified threshold then make up a proximity network.

13
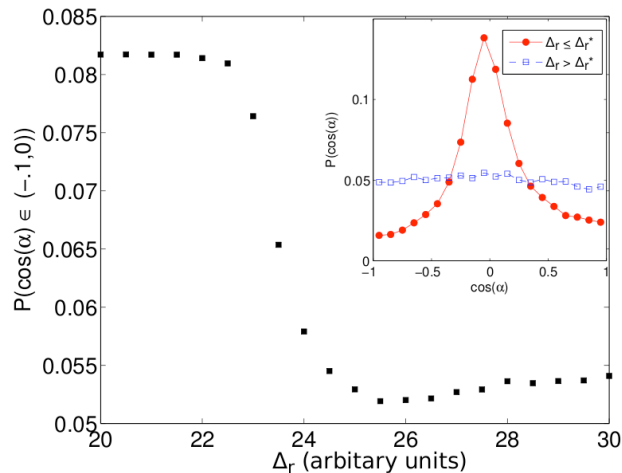
Figure 2.2: The peak value of the α cosines, $P[\cos(\alpha)]$ as a function of radial displacement Δ_r. Smaller peak values indicate more uniform distributions. Note the sudden decrease to uniformity as the radial displacement increases. We take the value after the sudden decrease ($\Delta_r^* = 24.5$) as our conservative upper bound on particle contact distance. Inset: The distribution of $P[\cos(\alpha)]$ for touching $\Delta_r \leq 24.5$ [circles] and non-touching $\Delta_r > 24.5$ [squares] particles.

2.4   Network Analysis

In order to capture the dynamics of the granular flow, we study the time-evolving broken-links network. A link is considered 'broken' relative to some reference frame if the particles it linked in the reference time frame move away from each other some time later (i.e. no longer meet the criterion for assigning contacts). Thus, the time evolving broken-links network is the collection of all such links (and the nodes/particles they are attached to). A schematic of this operation is displayed in Figure 2.3a. To lower the occurrence of false rearrangement events, in order for

a link to break, it must be broken in the current frame as well as the subsequent frame. We do not allow links to reform once they have been broken.
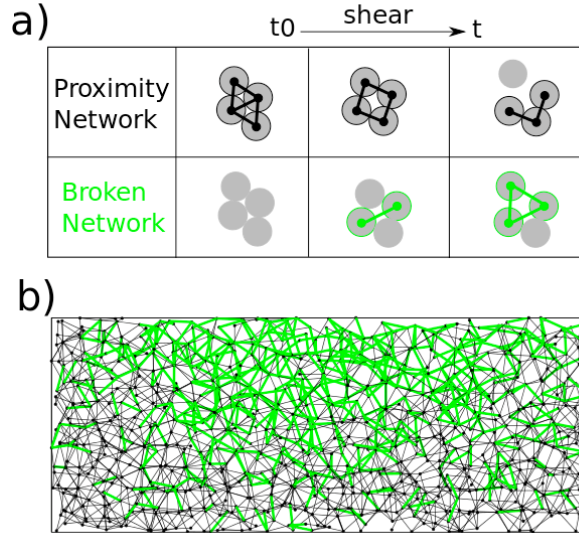
Figure 2.3: (a) A schematic of the definition and growth of the broken-links network. b) Example cross section of the broken [green/light gray] and persistent [black] networks, plotted in real space.

We choose to focus on the broken network because we are primarily interested in the propagation of fracture events. However, in other applications, it may be instructive to consider the complimentary network of persistent links, defined as the set particles that are linked in the reference frame and remain in contact for all subsequent frames. Figure 2.3b illustrates the complementarity between the broken network and the persistent network.

In addition to considering the experimentally determined broken network, we implement a model of link breakages where the probability of a link breaking is

proportional to the average rate of longitudinal strain (elongation) in the direction of the edge. Using the actual experimentally measured positions of the particles, we begin by choosing a reference time and consider the contact network present at that time. To consider the effect of increasing shear, we take the experimental particle positions after the shear has been applied and for each edge in the reference network, find $\vec{r'}$ the position of the midpoint between the particle centers. Thus, $\vec{r'}$ serves as an approximation for the location of the edge in the shear cell, even if the particles have moved away from each other.

Since the dominant average velocity is in the angular direction and uniform as a function of angle, we can approximate $\vec{v} = (v_r, v_\theta, v_z) = (0, r\omega(r,z), 0)$, and calculate both the strain rate tensor $\mathbf{D}$, and the rate of longitudinal strain,

$$\dot{\epsilon} = \hat{e} \cdot \mathbf{D} \cdot \hat{e} \tag{2.1}$$

$$= (\hat{\theta} \cdot \hat{e}) \left[r\frac{\partial \omega}{\partial r}(\hat{r} \cdot \hat{e}) + r\frac{\partial \omega}{\partial z}(\hat{z} \cdot \hat{e}) \right]_{\vec{r'}} \tag{2.2}$$

where $\hat{r}$ is taken relative to the center of the disk and $\hat{e}$ is the unit vector from one particle center to the other. For each amount of shear considered, we define the probability of breaking a link in the contact network, p, to be

$$p \propto \dot{\epsilon}\Theta(\dot{\epsilon}) \tag{2.3}$$

where Θ is the Heaviside step function. Thus, we only assign probabilities of breaking to edges that have positive longitudinal strain (particles moving apart). Linear interpolation is used to evaluate the velocity gradients. The probability of breaking is normalized such that the expected value of the fraction of edges broken, f_b, after

16

each amount of shear is applied is equal to the experimentally observed value, as seen in Figure 2.4a. We also implement the model described above with noise. For a given amount of shear, a number M_b of the reference edges must be broken in order to match the experimentally observed fraction broken, f_b. We introduce a noise parameter $0 \leq \eta \leq 1$ such that $M_b\eta$, of these edges are broken according to Eq (2.3), and the remaining $(1 - \eta)M_b$ edges are broken randomly with uniform probability.

A particularly useful metric to capture the growth of the broken-links network is the size of its giant component. The giant component is the largest collection of connected nodes and edges present in the broken network at any given time. In network theory, it is the order parameter that signifies a phase transition in the behavior of the system [29, 30]. The size of the giant component, s_g, is the fraction of nodes from the reference graph that are in the giant component. Thus, as shear is applied, one would expect the giant component of the broken network to grow in time.

The optimal value of η is found by maximizing the agreement between the model and the experimental data. A subset of the reference networks is used to calculate the giant component size as a function of shear, and η is tuned to minimize the mean squared difference between the calculated and experimental curves.

We consider one set of constant shear with a total of 240 frames, corresponding to 717 degrees of rotation of the bottom plate. The first 210 frames are each taken as a reference frame and define 210 proximity networks. We allow particle tracks to be considered valid if the largest number of consecutive untracked frames for

17
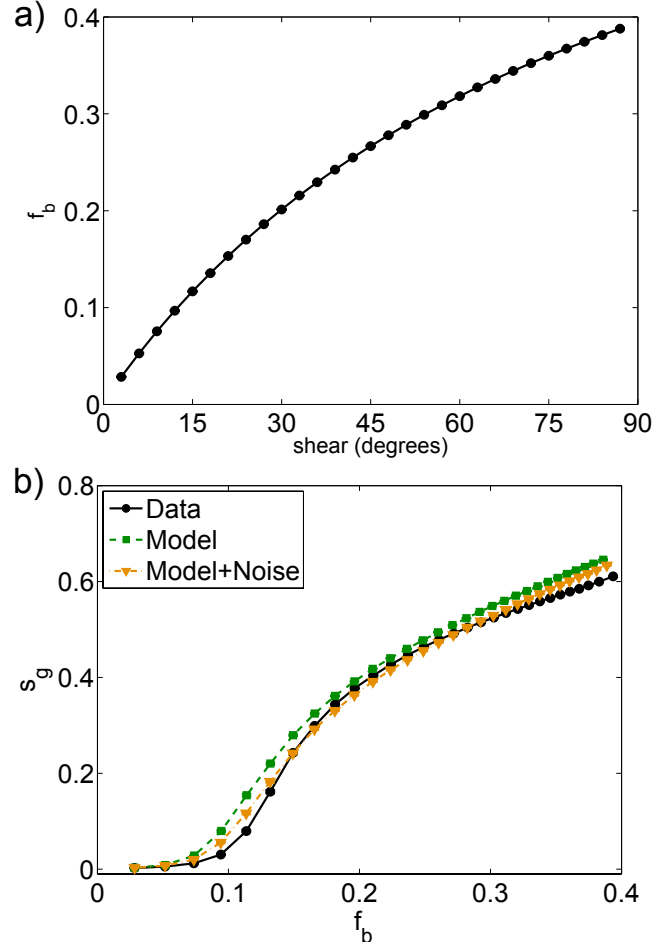
Figure 2.4: (a) The fraction of edges broken as a function of applied shear for the experimental data, averaged over all reference networks. (b) The size of the giant component s_g as a function of the fraction of broken edges for the experimental data [circles], longitudinal strain model [squares], and the longitudinal strain model with noise ($\eta = 0.84$) [triangles]. Errorbars represent the standard error and are smaller than the markers.

that particle is less than or equal to one. This condition is necessary since the experimental data contain some gaps, i.e. particles are not detected in some frames. For each network, the growth of the broken-links network and the giant component

18

is studied over the subsequent 87 degrees, and we only consider particles whose tracks are valid for those 87 degrees.

We average over all 210 reference networks. Figure 2.4 plots the result of this analysis, with the size (number of nodes) of the giant component (relative to the reference network) as a function of the fraction of edges broken, f_b. It is clear that the fraction of edges broken, f_b, plays the role of a tuning parameter, in the same way that an occupation probability is used to tune the behavior of a percolating system. The data suggest a continuous phase transition in the size of the giant component. One can map the fraction of edges broken to strain, via Figure 2.4a. Thus, one can map the value of f_b at which the giant component forms to a characteristic strain scale corresponding to the onset of global fracture, $s_{char} \sim 15$ degrees.

Continuing the analogy with a percolation phase transition, we can look for a measure associated with a correlation length. To this end, we plot the average non-giant cluster size as a function of f_b in Figure 2.5a. Note that mean cluster size peaks approximately in the region in which the transition appears to occur in Figure 2.4b. We can further investigate this transition by looking at the cumulative distribution of cluster sizes at f_b values near this peak. The cumulative size distribution $P(s' \geq s)$ is the probability that a cluster has a size s' greater than or equal to s. Figure 2.5b plots the cumulative size distribution of clusters for three different ranges in f_b: a f_b range well before the transition, a range close to the transition (corresponding to values near the peak of $\langle s \rangle$), and a range well after the transition. We immediately note that the distribution of cluster sizes for a range near the transition is much heavier tailed than both distributions before or after the transition, as one would

expect for a percolation like transition.
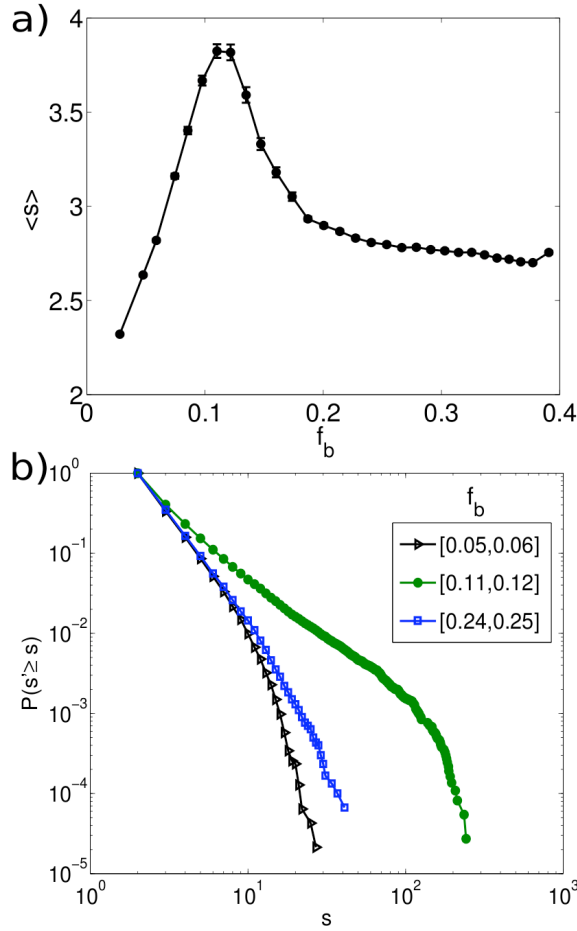
Figure 2.5: (a) The average non-giant cluster size as a function of the fraction of broken edges f_b for the experimental data. (b) The cumulative size distribution for the non-giant components taken at three different ranges of f_b: $0.05 \leq f_b \leq 0.06$ [lower triangles], $0.11 \leq f_b \leq 0.12$ [upper circles], $0.24 \leq f_b \leq 0.25$ [middle squares].

Additionally, we can investigate the structure of the broken-links network as it grows by computing the network's clustering coefficient, which reflects the extent to which neighbors of a node are themselves neighbors. The clustering coefficient

for a node j is defined as

$$c_j = \frac{2T(j)}{(k_j)(k_j - 1)}$$

where k_j is the degree of node j, the number of neighbors, and the number of triangles $T(j)$ is the number of pairs of neighbors of j that are also linked to each other in the broken link network. The clustering coefficient measures the fraction of possible triangles centered at node j that are observed. The network clustering coefficient is simply the average over all nodes of the nodes' clustering coefficients $C = \langle c_j \rangle$ [36]. Thus, a larger value of C for the broken-links network means that particle contacts tend to break more between nodes whose contacts have broken previously. Figure 2.6 plots the average clustering coefficient as a function of the fraction of edges broken averaged over all runs. We note that both the model and the model with noise are less clustered than the data. Thus, while it appears that the model and model with noise appear to qualitatively reproduce the transition of the giant component, they fail to fully capture the structure of the data.
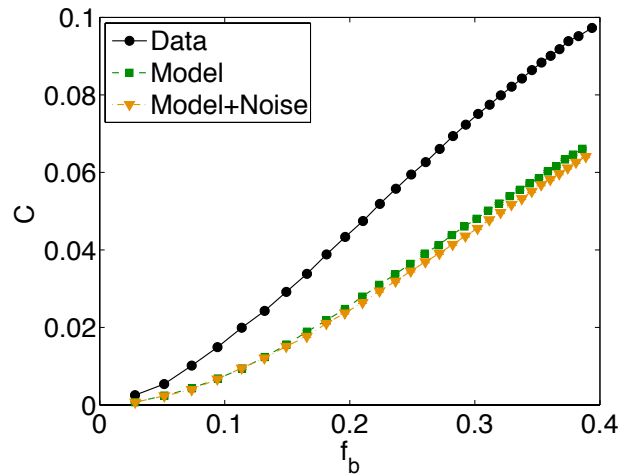
Figure 2.6: The clustering coefficient C, as a function of the fraction of edges broken, averaged over all reference networks. Bins are selected such that each bin contains the same number of data points. Error bars represent the standard error and are smaller than the markers. The experimental data [upper circles] are more clustered than both the model [squares] and the model with noise [triangles].

2.5 Expression for Longitudinal Strain

We present here a short derivation for the rate of strain used in our model expression, Eq. (2.2). Assuming that the velocity of the flow is given as:

$$\vec{v} = (0, r\omega(r, z), 0) \tag{2.4}$$

i.e. the dominant portion of the flow is in the angular direction and is uniform in θ, one can calculate the elements of the strain rate tensor in cylindrical coordinates [37]:

$$D_{rr} = \frac{\partial v_r}{\partial r} = 0 \tag{2.5}$$

$$D_{r\theta} = \frac{1}{2} \left(\frac{1}{r} \frac{\partial v_r}{\partial \theta} + \frac{\partial v_\theta}{\partial r} - \frac{v_\theta}{r} \right) \tag{2.6}$$

$$= \frac{1}{2} \left(r \frac{\partial \omega}{\partial r} + \omega - \omega \right)$$

$$= \frac{1}{2} r \frac{\partial \omega}{\partial r}$$

$$D_{rz} = \frac{1}{2} \left(\frac{\partial v_r}{\partial z} + \frac{\partial v_z}{\partial r} \right) = 0 \tag{2.7}$$

$$D_{\theta\theta} = \frac{1}{r} \frac{\partial v_\theta}{\partial \theta} + \frac{v_r}{r} = 0 \tag{2.8}$$

$$D_{\theta z} = \frac{1}{2} \left(\frac{1}{r} \frac{\partial v_z}{\partial \theta} + \frac{v_\theta}{\partial z} \right) \tag{2.9}$$

$$= \frac{1}{2} r \frac{\partial \omega}{\partial z}$$

$$D_{zz} = \frac{\partial v_z}{\partial z} = 0 \tag{2.10}$$

Then, the rate of elongation per unit length is then $\dot{\epsilon}$ in the direction $\hat{e}$:

$$\dot{\epsilon} = \hat{e} \cdot D \cdot \hat{e} \tag{2.11}$$

$$= \begin{bmatrix} e_r & e_\theta & e_z \end{bmatrix} \frac{1}{2} r \begin{bmatrix} 0 & \dfrac{\partial \omega}{\partial r} & 0 \\[2mm] \dfrac{\partial \omega}{\partial r} & 0 & \dfrac{\partial \omega}{\partial z} \\[2mm] 0 & \dfrac{\partial \omega}{\partial z} & 0 \end{bmatrix} \begin{bmatrix} e_r \\[2mm] e_\theta \\[2mm] e_z \end{bmatrix}$$

$$= r \left(e_r e_\theta \frac{\partial \omega}{\partial r} + e_\theta e_z \frac{\partial \omega}{\partial z} \right)$$

$$= r(\hat{e} \cdot \hat{\theta}) \left[(\hat{e} \cdot \hat{r}) \frac{\partial \omega}{\partial r} + (\hat{e} \cdot \hat{z}) \frac{\partial \omega}{\partial z} \right].$$

2.6 Comment on Choice of Δ_r^*

As described above, the value for the proximate distance cutoff Δ_r^* is found via investigating the behavior of $p(\alpha)$, see Fig. 2.2. It is natural then to ask how sensitive these results are on the choice of Δ_r^*. To investigate, we reran the analysis with two other choices of cutoff, $\Delta_r^* = 23.5$ and $\Delta_r^* = 25.5$. As one would expect, for smaller Δ_r^* the as the system is sheared, links are more likely to break then compared to larger values of Δ_r^*. Additionally, the value of f_b at which a giant component forms is altered by the choice of Δ_r^*: smaller values of Δ_r^* have giant component formation at larger values of f_b. Moreover, when comparing different values of Δ_r^*, one should compare the control parameter, the amount of applied shear. Plotting giant component size as a function of time in Fig. 2.7 we see that the onset of giant component formation is ~ 15 degrees for all three choices in Δ_r^*.
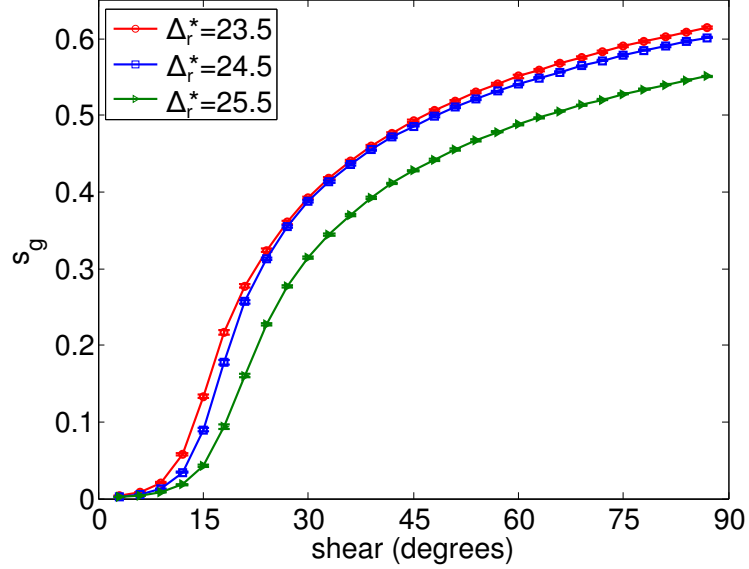
Figure 2.7: The values of s_g as a function of applied shear for three different values of Δ_r^* red (circles): $\Delta_r^* = 23.5$, blue (squares): $\Delta_r^* = 24.5$, green (triangles) $\Delta_r^* = 25.5$

2.7   Summary and Conclusions

Shear zones and reproducible flow fields are a key feature of granular flows. In order to capture dynamics between particle and bulk scales, we introduced a new, complex networks approach to studying the dynamics of granular flow: the time-evolving broken-links network. A transition reminiscent of a phase transition in percolation is observed: a giant component of this network develops as shear is applied to this system. The appearance of this giant component reflects the onset of global fracture in the sense that the breaks in the original proximity network start to become globally connected. Additionally, we note a peak in the mean component size in proximity to the observed transition, as well as a heavy tailed distribution in the component size. This heavy-tailed length scale distribution is

reminiscent of the one observed in string-like dynamics [24]. The network approach used here is ideal for studying granular phenomenon that exhibit a diverging length scale of this type. Our work shows that even in the case of a diverging length scale, it is possible to recover a characteristic strain scale corresponding to the onset of global fracture. We hypothesize that this strain scale can be linked to physical features of the system such as the loss of reversibility (this is the focus of ongoing work). Comparison to a model of link breakages, in which breakage events depend on the average longitudinal strain, highlights the collective nature of dense granular shear flows: the experimental data's broken-links network exhibits a larger clustering coefficient, indicating a more localized fracture than the model. This suggests that in a granular shear flow, breakage of a link between particles increases the likelihood of breakage of other nearby links. This further implies that the rearrangement events are cooperative. Indeed there is evidence for collective dynamics in dense granular flows, for example collective roll-like dynamics seen in chute flows [38] and string like rearrangements in excited dense granular materials [39]. The network analysis provides a characteristic strain scale at which the network topology changes specifically without the need to focus on a particular lengthscale for collective dynamics. In conclusion, we believe that a dynamic networks approach offers a novel method to quantify granular flows at intermediate scales.

Chapter 3

Echoes and Revival Echoes in Systems of Anharmonically Confined

Atoms

3.1 Abstract

We study echoes and what we call 'revival echoes' for a collection of atoms
that are described by a single quantum wavefunction and are confined in a weakly
anharmonic trap. The echoes and revival echoes are induced by applying two,
successive temporally localized potential perturbations to the confining potential,
one at time $t = 0$, and a smaller one at time $t = \tau$. Pulse-like responses in the
expectation value of position $\langle x(t) \rangle$ are predicted at $t \approx n\tau$ $(n = 2, 3, \ldots)$ and
are particularly evident at $t \approx 2\tau$. While such echoes are familiar from previous
work, a result of our study is the finding of 'revival echoes'. Revivals (but not
echoes) occur even if the second perturbation is absent. In particular, in the absence
of the second perturbation, the response to the first perturbation dies away, but
then reassembles, producing a response at revival times mT_x $(m = 1, 2, \ldots)$. The

existence of such revivals is due to the discreteness of the quantum levels in a weakly anharmonic potential, and has been well-studied previously. If we now include the second perturbation at $t = \tau$, we find temporally localized responses, *revival echoes*, both *before* and after $t \approx mT_x$, e.g., at $t \approx mT_x - n\tau$ (pre-revival echoes) and at $t \approx mT_x + n\tau$, (post-revival echoes), where m and n are $1, 2, \ldots$. One notable point is that, depending on the form of the perturbations, the 'principal' revival echoes at $t \approx T_x \pm \tau$ can be much larger than the echo at $t \approx 2\tau$. We develop a perturbative model for these phenomena, and compare its predictions to the numerical solutions of the time-dependent Schrödinger equation. The scaling of the size of the various echoes and revival echoes as a function of the symmetry of the perturbations applied at $t = 0$ and $t = \tau$, and of the size of the external perturbations is investigated. The quantum recurrence and revival echoes are also present in higher moments of position, $\langle x^p(t) \rangle$, $p > 1$. Recurrences are present at $t \approx mT_x/j$, and dominant pre and post-revival echoes occur at fractional shifts of τ, i.e. $t \approx (mT_x \pm \tau)/j$, where the $m = 1, 2, \ldots$ and the integer values of j are determined by p. Additionally, we use the Gross-Pitaevskii equation to study the effect of atom-atom interactions on these phenomena. We find that echoes and revival echoes become more difficult to discern as the size of the second perturbation is increased and/or as the atom-atom interactions become stronger.

3.2 Introduction

In both classical and quantum systems with nonlinearity, a distribution of oscillation frequencies leads to dephasing of the response to a temporally localized system perturbation and to damping in physical observables of the response. After this response damps away, application of another external perturbation can induce subsequent build up of phase coherence, causing later temporally localized responses, called *echoes*. Examples have been investigated in nuclear magnetic resonance (spin echoes) [40], coupled oscillators [41], plasma physics [42–44], cavity quantum electrodynamics [45, 46], and cold atom systems [47–52]. Additionally, in quantum mechanical systems, another phenomena, the so called *revivals* due to the discreetness of the energy eigenstates, can occur [53–55]. Revivals are also present in systems with a Jaynes-Cummings type interaction, and have been studied both theoretically [56, 57], and experimentally in trapped-ion [58], cavity QED [59], and circuit QED [60] systems. In particular, revivals are macroscopic responses that can result due to reconstruction of phase coherence in the absence of the second perturbation. Previous work has investigated, both experimentally and theoretically, revival [53], and echo phenomena in trapped atomic systems induced by changes in depth [47], or translations of [49, 50], the confining potential.

Here we consider echo phenomena induced by two impulsive, successive external perturbations applied to a collection of atoms in a weakly anharmonic trap. For example, the type of external perturbation that we consider in most detail is the application of two translations to the trapping potential, one at time $t = 0$, and a

29

smaller translation at time $t = \tau$. We study the response of the expectation value of position $\langle x(t) \rangle$. In the case of a Bose-Einstein condensate confined by the pondermotive force of a laser beam, translations of the potential can be realized by switching of the laser beam position, or by a change in phase of two interfering beams [49]. As in previous work [47, 49, 50], this method results in the creation of echoes, e.g., at $t \approx 2\tau$, and in the quantum mechanical revival described in [53–55] at, e.g., $t \approx T_x$. In addition, however, we also find quantum 'revival echoes' occurring both *before* and after the revival, e.g., at $t \approx T_x \pm \tau$ and $t \approx T_x \pm 2\tau$. Furthermore, we find that these revival echoes can have much larger amplitudes than, say the echo at $t \approx 2\tau$ (conditions for this to be the case are discussed in Sec. 3.4). In Sec. 3.3 we develop a quantum mechanical, perturbative model (in the limit of small anharmonicity and small second displacement) for echoes and revival echoes. We then compare these results to the numerically solved, time dependent Schrödinger equation. We study the behavior of echoes and revival echoes at different choices of anharmonicity and time delay τ, as well as how the size of the various echoes scale with the size of the external perturbations. In Sec. 3.4 we discuss what effect the spatial symmetry of the external stimuli has on the echo phenomena, in particular the echoes' relative sizes. In Sec. 3.5 the quantum recurrence and revival echoes are investigated in higher moments of position, $\langle x^p(t) \rangle$, $p > 1$. Recurrences are present at $t \approx mT_x/j$, and dominant pre and post-revival echoes occur at fractional shifts of τ, i.e. $t \approx (mT_x \pm \tau)/j$, where $m = 1, 2, \ldots$ and the integer values of j are determined by p. Lastly, we model atom-atom interactions in our system using the Gross-Pitaevskii equation, and study the effect of interactions on the revival echo

phenomena (Sec. 3.6).

The previous references most closely related to our work are the Refs. [47–52] on echoes in systems of confined atoms, none of which find our revival echoes. Reference [47] presents a theoretical treatment of echoes in confined, cold atoms induced by successive changes in the depth of the confining potential. Reference [48] theoretically and numerically studies the echo phenomena in a Bose-Einstein condensate where the dephasing is reversed with an external optical potential. Reference [49] reports on experimental observations of echoes induced by sudden shifts of the potential well realized by changing the relative phasing of interfering laser beams, while Ref. [50] experimentally and numerically compares the effectiveness of translations with different temporal profiles in creating echoes. Reference [51] experimentally observes an echo in a collection of trapped atoms induced by applying a short microwave π pulse, where the echo is measured via Ramsey spectroscopy. Reference [52] numerically implements a Bose-Hubbard model to describe a collection of atoms in an optical lattice and their echo response to pulses of radiation in the presence of atom-atom interactions.

3.3   Model and Numerical Results

We begin by looking at echo phenomena present in the absence of atom-atom interactions. We study the quantum evolution of an initially Gaussian state in a

weakly anharmonic, one-dimensional trap,

$$i\frac{\partial}{\partial t}\psi = (H_0 + H_1)\psi, \tag{3.1}$$

$$H_0 = -\frac{1}{2}\frac{\partial^2}{\partial x^2} + \frac{1}{2}x^2, \tag{3.2}$$

$$H_1 = \frac{1}{4}\beta x^4, \tag{3.3}$$

where β quantifies the anharmonicity of the trap, with $\beta \ll 1$. We use harmonic units, $x = \bar{x}/(\sqrt{\hbar/m\omega_0})$, $t = \omega_0\bar{t}$, where $\bar{x}$ and $\bar{t}$ are the unnormalized units, ω_0 is the frequency of the harmonic oscillator, and m is the mass. The procedure will be the following.

1. Begin with a Gaussian wavepacket centered $x = 0$.

2. At $t = 0$ translate the state by an amount d_1, $x \to x + d_1$.

3. At $t = \tau$ translate the state again in x by an amount d_2.

Later (Sec. 3.4) we will discuss another type of perturbation that is not a translation, and we will find that the spatial symmetry of the perturbations can have important effects. In order to most clearly stimulate echoes, revivals, and revival echoes, we will initially take $d_2 \ll 1$. We first seek the frequencies ω_n of our anharmonic Hamiltonian, $H = H_0 + H_1$, for H_1 (i.e., β) small. Expanding ω_n to second order in β, we write

$$\omega_n = \omega_n^{(0)} + \delta\omega_n^{(1)} + \delta\omega_n^{(2)}. \tag{3.4}$$

The corrections to the frequencies are conveniently calculated using the creation/annihilation formalism of the harmonic oscillator.

$$\hat{x} = \sqrt{\frac{1}{2}}(\hat{a}^\dagger + \hat{a}), \tag{3.5}$$

$$\hat{p} = i\sqrt{\frac{1}{2}}(\hat{a}^\dagger - \hat{a}), \tag{3.6}$$

$$\hat{a}|n\rangle = \sqrt{n}|n-1\rangle, \tag{3.7}$$

$$\hat{a}^\dagger|n\rangle = \sqrt{n+1}|n+1\rangle, \tag{3.8}$$

Taking $H_1 = (\beta/16)(\hat{a}^\dagger + \hat{a})^4$, perturbation theory [61] yields

$$\delta\omega_n^{(1)} = \langle n|H_1|n\rangle = \frac{\beta}{16}(3 + 6n(1+n)), \tag{3.9}$$

$$\delta\omega_n^{(2)} = \sum_{k \neq n} \frac{|\langle n|H_1|k\rangle|^2}{(n+1/2) - (k+1/2)}. \tag{3.10}$$

$$= \frac{\beta^2}{256}\left\{ \left[2n(1-2n)^2(n-1)\right]\Theta(n-2) + \left[\frac{1}{4}n(n^3 - 6n^2 + 11n - 6)\right]\Theta(n-4) \right.$$

$$\left. - 2(2 + 3n + n^2)(3 + 2n)^2 - \frac{1}{4}(2 + 3n + n^2)(n^2 + 7n + 12) \right\},$$

where $H_0|n\rangle = \omega_n^{(0)}|n\rangle$ defines the state $|n\rangle$ of the unperturbed harmonic oscillator, and $\Theta(n) = 1$ for $n \geq 0$ and $\Theta(n) = 0$ for $n < 0$. The position translations described in the procedure can be implemented using the unitary translation operator,

$$T(d) = \exp[-i\hat{p}d], \tag{3.11}$$

where d is the displacement size, $d = d_1$ or $d = d_2$. The matrix elements of this operator in the harmonic oscillator basis are

$$\langle m|T(d)|n\rangle = \exp\left[-\frac{\gamma^2}{2}\right] \sum_{q=0}^{n} \frac{(-\gamma)^q \gamma^{m-n+q}\sqrt{n!}\sqrt{m!}}{(m-n+q)!(n-q)!q!}\Theta(m-n+q), \tag{3.12}$$

33

where $\gamma = d/\sqrt{2}$. There are two special cases of Eq. (3.12) that will be useful in our analysis. The first is the displacement of the harmonic oscillator ground state $|n\rangle = |0\rangle$ (a Gaussian wavepacket centered at $x = 0$),

$$\langle m|T(d)|0\rangle = \exp\left[-\frac{\gamma^2}{2}\right]\frac{\gamma^m}{\sqrt{m!}} \equiv \exp\left[-\frac{\gamma^2}{2}\right]C(m,\gamma), \tag{3.13}$$

where $C(m,\gamma) = \gamma^m/\sqrt{m!}$. This expression is the well known coefficient for a coherent state formed by displacing the harmonic oscillator ground state.

The second useful expression is the case when $\gamma\sqrt{n} \ll 1$. In this case, we can approximate the matrix element as

$$\langle m|T(d)|n\rangle = \exp\left[-\frac{\gamma^2}{2}\right]\Big[\delta_{m,n} + \delta_{m,n+1}\gamma\sqrt{n+1} - \delta_{m,n-1}\gamma\sqrt{n}\Theta(n-1) \tag{3.14}$$

$$- \delta_{m,n}\gamma^2 n\Theta(n-1) + \frac{\delta_{m,n+2}}{2}\gamma^2\sqrt{(n+1)(n+2)}$$

$$+ \frac{\delta_{m,n-2}}{2}\gamma^2\sqrt{n(n-1)}\Theta(n-2) + \mathcal{O}(\gamma^3)\Big]$$

noting that small displacements predominantly excite nearby states.

We first consider the response of the system due to an initial displacement at $t = 0$. Beginning with the harmonic oscillator ground state ($|\psi\rangle = |0\rangle$) at $t = 0$, we apply a displacement d_1. Using the described approximations for the frequencies, and, approximating the eigenstates as the unperturbed states $|n\rangle$, for a time $0 < t < \tau$, the quantum state is

$$|\psi(t < \tau)\rangle = \exp\left[-\frac{\gamma_1^2}{2}\right]\sum_n C(n,\gamma_1)\exp[-i\omega_n t]|n\rangle. \tag{3.15}$$

After the displacement d_1, the probability of being in the n-th state is $\exp[-\gamma_1^2]C(n,\gamma_1)^2$, a Poisson distribution with mean,

$$\bar{n} = \gamma_1^2, \tag{3.16}$$

and variance

$$\sigma_n^2 = \bar{n} = \gamma_1^2. \tag{3.17}$$

(Physically, the value of $\bar{n}$ is given as the classical energy over the harmonic oscillator frequency, $\omega_0 = 1$, $\bar{n} = (p^2/2 + x^2/2)/\omega_0 = d_1^2/2 = \gamma_1^2$.)

The response of the system, as measured by the expectation value, $\langle \psi | x | \psi \rangle$, is given by

$$\frac{\langle x(t) \rangle}{2A^2/\sqrt{2}} = \sum_{n=0}^{\infty} C(n)C(n+1)\sqrt{n+1}\cos[(\omega_{n+1} - \omega_n)t], \tag{3.18}$$

where for notational clarity we have dropped γ_1 in the argument of $C(n) = C(n, \gamma_1)$, and $A = \exp[-\gamma_1^2/2]$.

For comparison, we obtained numerical solutions of the Scrödinger Equation using a split-step operator method [17]. Figure 3.1(a) shows a plot of $\langle x(t) \rangle$ versus t obtained by numerical solution of the Schrödinger equation in the absence of the second displacement. We see from Fig. 3.1(a) that the displacement at $t = 0$ leads to a fast oscillatory response whose envelope decays to small values by $t \sim 1500$. At longer time, the response reassembles with its envelope reaching a peak value at the 'revival time' $T_x \cong 8625$. This revival of the response has been called a quantum revival or recurrence. (Note that in Fig. 3.1 the fast oscillations are not visible because the thickness of the line that is plotted exceeds the period of the fast oscillations.) Figure 3.1(b) plots the value of $\langle x(t) \rangle$ calculated from Eq. (3.18) with Eqs. (3.4), (3.9) and (3.10) used for the frequencies. We note very good agreement between the model and the numerical solution.

As we now verify, this term includes the well known quantum recurrence [53–55]. (The expression for Eq. (3.18) does not capture the fractional revival described in [62,63]. This revival is much smaller in amplitude than the large revival at $t \approx T_x$, and is not visible on the scale used in Fig. 3.1. We have verified that a model including $\mathcal{O}(\beta)$ corrections to the energy eigenstates does reproduce these small fractional revivals). In order to estimate the quantum recurrence time of $\langle x(t) \rangle$, in a manner similar to Refs. [54, 55], we expand our expression for the frequency difference around a mean value of n, denoted by $\bar{n}$. Using Eqs. (3.9) and (3.10), the energy difference between two adjacent states can be approximated as

$$\omega_{n+1} - \omega_n \approx \Delta\omega_{\bar{n}} + a(n - \bar{n}) + ..., \tag{3.19}$$

where

$$\Delta\omega_{\bar{n}} = 1 + \frac{3}{4}\beta(\bar{n} + 1) + \beta^2 \left(\frac{9}{8} + \frac{51}{32}\bar{n} + \frac{51}{64}\bar{n}^2 \right) \tag{3.20}$$

$$a = \frac{3}{32}(8\beta - 17\beta^2 - 17\bar{n}\beta^2). \tag{3.21}$$

$\Delta\omega_{\bar{n}}$ is the difference in the two energies, evaluated at $\bar{n}$ (and is independent of n). We can then express $\cos[(\omega_{n+1} - \omega_n)t]$ as:

$$\cos[(\Delta\omega_{\bar{n}} + a(n - \bar{n}))t] \cong Re\big\{ \exp[i\Delta\omega_{\bar{n}}t] \exp[ia(n - \bar{n}))t] \big\}. \tag{3.22}$$

In the vicinity of $\bar{n}$, the oscillatory behavior is a product of a fast oscillation at a frequency $\Delta\omega_{\bar{n}}$, which is independent of n, and a slow oscillation, which is periodic for all n at a period $2\pi/a$. Thus the envelopes are periodic at times $t = mT_x$ ($m = 1, 2, ...$) where

$$T_x = \frac{2\pi}{a}, \tag{3.23}$$

36

which agrees with the value $T_x \cong 8625$ estimated by inspection of Fig. 3.1(a).

It should also be noted that the time $T_x \approx T_{rev}/2$, where T_{rev} is the revival time it takes the state to come back to approximately its initial condition. The recurrence in $\langle x(t) \rangle$ corresponds to a mirror revival [55], e.g.: the quantum state has reassembled as a mirror image of its initial condition on the opposite side of the anharmonic well.
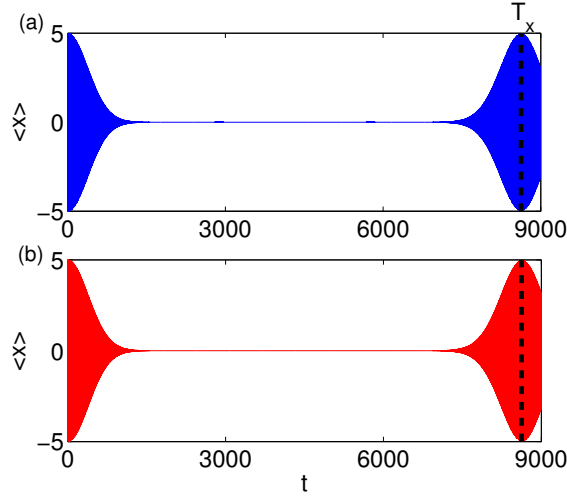
Figure 3.1: **(a):** $\langle x(t) \rangle$ found through numerical solution of the Schrödinger equation for a system with only one initial displacement at $t = 0$. $\beta = 0.001$, $d_1 = 5$. **(b):** $\langle x(t) \rangle$ found through the perturbative model, for the same parameters as (a). Note good agreement between the model and the numerical solution.

Now, including the effect of the second displacement, the state is allowed to evolve to time $t = \tau$, at which time it experiences a small second displacement by an amount d_2. In order to utilize the expression in Eq. (3.14) we define $\gamma_2 = d_2/\sqrt{2}$ and require $\gamma_2 \sqrt{n} \ll 1$. Taking as an upper bound on n to be $\bar{n} + 3\sigma_n$, and noting

37

that $\bar{n} = \gamma_1^2$ we require $\gamma_2 \ll (\gamma_1^2 + 3\gamma_1)^{-1/2}$. Using the expression for $\langle m|T(d)|n\rangle$ in Eq. (3.14) we find

$$|\psi(t > \tau)\rangle = \exp\left[-\frac{\gamma_1^2}{2}\right] \sum_{m,n} \langle m|T(d_2)|n\rangle C(n) \exp[-i\omega_n\tau] \exp[-i\omega_m(t-\tau)]|m\rangle$$

$$(3.24)$$

$$\approx A\Bigg\{ \sum_{m=0}^{\infty} C(m)\exp(-i\omega_m t)|m\rangle \qquad (3.25)$$

$$+ \gamma_2 \sum_{m=1}^{\infty} C(m-1)\sqrt{m}\exp[-i\omega_{m-1}\tau]\exp[-i\omega_m(t-\tau)]|m\rangle$$

$$- \gamma_2 \sum_{m=0}^{\infty} C(m+1)\sqrt{m+1}\exp[-i\omega_{m+1}\tau]\exp[-i\omega_m(t-\tau)]|m\rangle$$

$$- \gamma_2^2 \sum_{m=1}^{\infty} C(m)m\exp[-i\omega_m t]|m\rangle$$

$$+ \frac{\gamma_2^2}{2} \sum_{m=2}^{\infty} C(m-2)\sqrt{m(m-1)}\exp[-i\omega_{m-2}\tau]\exp[-i\omega_m(t-\tau)]|m\rangle$$

$$+ \frac{\gamma_2^2}{2} \sum_{m=0}^{\infty} C(m+2)\sqrt{(m+1)(m+2)}\exp[-i\omega_{m+2}\tau]$$

$$\times \exp[-i\omega_m(t-\tau)]|m\rangle + \mathcal{O}(\gamma_2^3)\Bigg\},$$

where $A = \exp\left[-(\gamma_1^2 + \gamma_2^2)/2\right]$. Using the expression for the quantum state for $t > \tau$, we can calculate the expectation value of the position $\langle x(t)\rangle = \langle \psi|x|\psi\rangle$ and order the terms in $\langle x(t)\rangle$ according to their dependence on the second displacement γ_2,

$$\langle x(t)\rangle = \langle x(t)\rangle^{(0)} + \langle x(t)\rangle^{(1)} + \langle x(t)\rangle^{(2)} + \dots \qquad (3.26)$$

The $0th$ order term $\langle x(t)\rangle^{(0)}$ is the result in the absence of the second displacement and is given by Eq. (3.18). Calculating the next highest term in γ_2 in our sum, we

find an expression for our first revival echo. which can be separated into two parts,

$$\langle x(t) \rangle^{(1)} = \langle x \rangle_1^{(1)} + \langle x \rangle_{-1}^{(1)}, \tag{3.27}$$

where

$$\frac{1}{\gamma_2} \frac{\langle x \rangle_1^{(1)}}{A^2/\sqrt{2}} = 2 \sum_{n=0}^{\infty} (n+1) \left\{ C(n)^2 - C(n+1)^2 \right\} \cos[(\omega_{n+1} - \omega_n)(t - \tau)], \tag{3.28}$$

and

$$\frac{1}{\gamma_2} \frac{\langle x \rangle_{-1}^{(1)}}{A^2/\sqrt{2}} = +2 \sum_{n=1}^{\infty} C(n+1)C(n-1)\sqrt{n(n+1)} \left\{ \cos\left[(\omega_{n+1} - \omega_n)t + (\omega_n - \omega_{n-1})\tau \right] \right.$$

$$\tag{3.29}$$

$$\left. - \cos\left[(\omega_{n-1} - \omega_n)t + (\omega_n - \omega_{n+1})\tau \right] \right\}.$$

The superscript refers to the power of γ_2 (ignoring the common dependence in the normalization constant A), and the subscript indicates the time of the echo, in units of τ, relative to $t = T_x$. For example, the first sum $\langle x \rangle_1^{(1)}$ has a cosine dependence similar to the quantum recurrence in Eq. (3.18), except t has been replaced with $t - \tau$. Thus, we expect a large amplitude in this second term at $t = \tau$ and $t \approx mT_x + \tau$ ($m \geq 1$), which we call a post-revival echo. The second sum $\langle x \rangle_{-1}^{(1)}$ has a time dependence which again depends on the difference of adjacent frequencies. Note however, that if we take the spacing between adjacent energy levels to be approximately independent of n, $\omega_{n+1} - \omega_n \approx \omega_n - \omega_{n-1}$, then $\cos[(\omega_{n+1} - \omega_n)t + (\omega_n - \omega_{n-1})\tau] \approx \cos[(\omega_{n+1} - \omega_n)(t + \tau)]$. Thus, we expect the second sum to contribute to a pre-revival echo at $t \approx mT_x - \tau$. Note that our expression for

$\langle x \rangle_{-1}^{(1)}$ only applies for $t > \tau$. Thus the m and τ values for pre-revival echoes are restricted by the requirement that $mT_x > 2\tau$ (e.g., for $\tau < T_x/2$ we have that $m \geq 1$ is permissible).

Continuing on to $\langle x(t) \rangle^{(2)}$, we can again separate this term by the location of the dominant echoes,

$$\langle x(t) \rangle^{(2)} = \langle x \rangle_0^{(2)} + \langle x \rangle_2^{(2)} + \langle x \rangle_{-2}^{(2)}, \tag{3.30}$$

where expressions for $\langle x \rangle_0^{(2)}$, $\langle x \rangle_2^{(2)}$, and $\langle x \rangle_{-2}^{(2)}$ are given in Appendix D.1.

With a similar argument for the time dependence of the first order terms, approximating the spacing between levels to be almost constant, each sum in $\langle x \rangle_0^{(2)}$ produces a second order response at $t \approx T_x$. Likewise, the second term $\langle x \rangle_2^{(2)}$ produces an echo at $t \approx 2\tau$ and a post-revival echo at $t \approx mT_x + 2\tau$, while pre-revival echoes from the last term $\langle x \rangle_{-2}^{(2)}$ occur at $t \approx mT_x - 2\tau$ ($m \geq 1$).

Figures 3.2 and 3.3 compare numerical solutions of the Schrödinger equation (Figs. 3.2(a,b) and Fig. 3.3(a)) with predictions (Figs. 3.2(c,d) and Fig. 3.3(b)) of the perturbation theory model [i.e., Eqs. (3.18), (3.26),(3.27)-(3.29), (D.1)-(D.4) for $\langle x(t) \rangle$, with Eqs. (3.4), (3.9), and (3.10) for ω_n] for different choices in β, τ, and d_2 parameters. In Fig. 3.2, $\langle x(t) \rangle$ is calculated for $\beta = 0.001$, $\tau = 1499$, $d_2 = 0.05$. There is good agreement between the numerics and the model, with the model reconstructing the quantum recurrence at $t \approx T_x$, and the echo and revival echoes at $t \approx 2\tau$, $t \approx T_x + \tau$, $t \approx T_x - \tau$ and $t \approx T_x - 2\tau$.

Similarly, Fig. 3.3 plots $\langle x(t) \rangle$ for a larger $\beta = 0.002$ and $d_2 = 0.1$, and a smaller value of $\tau = 1200$, showing more than one quantum revival echo. There is

again good agreement between the model and the numerics in capturing the behavior of the quantum recurrence at $t \approx mT_x$ $(m = 1, 2)$ and the echo and revival echoes at $t \approx 2\tau$, $t \approx mT_x - \tau$ and $t \approx mT_x - 2\tau$ $(m = 1, 2)$.
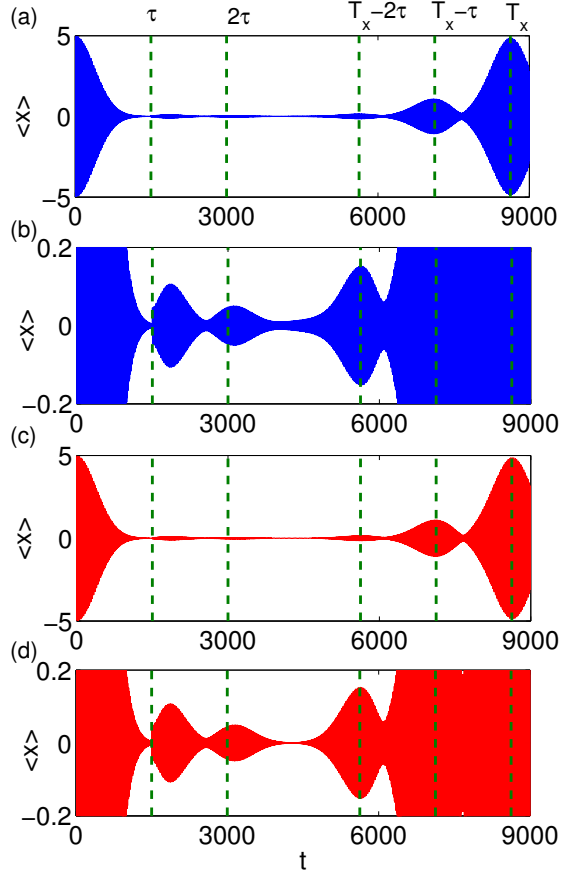
Figure 3.2: **(a):** $\langle x(t) \rangle$ solved numerically for the full Schrödinger equation for $\beta = 0.001$, $d_1 = 5$, $d_2 = 0.05$, $\tau = 1499$. **(b):** same as (a), but zoomed in to display the smaller echoes. **(c):** The model $\langle x(t) \rangle$ plotted for the same parameters. **(d):** same as (c), but zoomed in to display the smaller echoes. We note that the model reconstructs the $t \approx T_x - \tau$ pre-revival echo, as well as the echo at $t \approx 2\tau$ and the pre-revival echo at $t \approx T_x - 2\tau$.

41
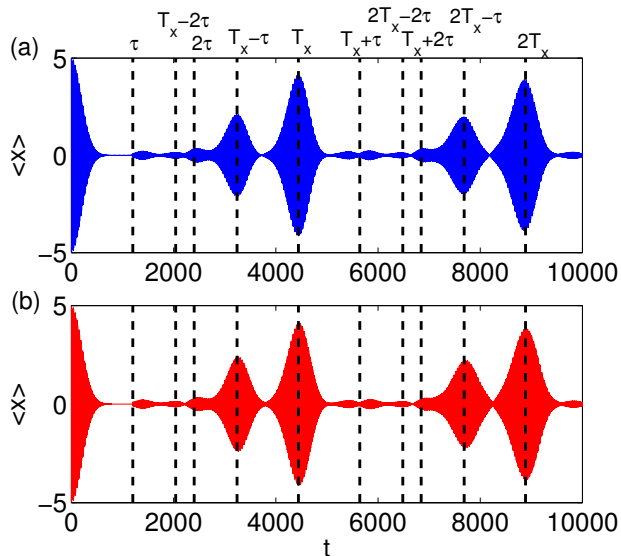
Figure 3.3: **(a)** $\langle x(t) \rangle$ solved numerically for the full Schrödinger equation for $\beta = 0.002$, $d_1 = 5$, $d_2 = 0.1$, $\tau = 1200$. **(b)** The model $\langle x(t) \rangle$ plotted for the same parameters. The model reconstructs the quantum recurrence at $t \approx T_x$, as well as the echo and revival echo responses at $t \approx 2\tau$, $t \approx T_x + \tau$, $t \approx T_x - \tau$, and $t \approx T_x - 2\tau$, $(m = 1, 2)$.

Additionally, the model indicates that one should expect the amplitude of the pre-revival echo a $t \approx T_x - \tau$ to scale linearly with the second displacement d_2. As seen in Eq. (3.28) the term $\langle x \rangle_1^{(1)}$ is proportional to γ_2 (and therefore d_2) if we ignore the weak dependence due to the normalization constant A. Similarly, the echo at $t \approx 2\tau$ and the pre-revival echo at $t \approx T_x - 2\tau$ (represented by $\langle x \rangle_2^{(2)}$ and $\langle x \rangle_{-2}^{(2)}$) are expected to increase quadratically with d_2, as shown in Eqs. (D.3) and (D.4) of Appendix D.1. We study the scaling of these echoes using the full numerical Schrödinger equation with the choice of $\beta = 0.001$, $\tau = 1899$, $d_1 = 5$, and various values of d_2. This value of τ is chosen to avoid the coincidence of the $t \approx 2\tau$ echo

and the $t \approx T_x - 2\tau$ pre-revival echo with the small fractional revival described in [62, 63]. The amplitudes of the echoes and pre-revival echoes as a function of d_2 are plotted in Fig. 3.4, and compared to the amplitude scaling predictions of the perturbative model. We note that indeed the pre-revival echo at $t \approx T_x - \tau$ appears to behave linearly with d_2, while the echo at $t \approx 2\tau$ and the pre-revival echo $t \approx T_x - 2\tau$ appear to grow quadratically, as expected. In general, the model suggests that echoes at $t \approx n\tau$ and revival echoes at $t \approx mT_x \pm n\tau$ ($m \geq 1$, $n \geq 1$) should have lowest order scalings of $(d_2)^n$. (It should be noted, however, that the scaling of very small echoes may be affected by revivals and echoes occurring due to corrections in the energy eigenstates.)

An approximate dependence of the pre-revival echo at $t \approx T_x - \tau$ on the first perturbation d_1 can also be obtained, and can be understood by studying Eq. (3.29). At the time of maximal $\langle x(t) \rangle$ (in the vicinity of $t \approx T_x - \tau$), one expects that for n near $\bar{n}$, the cosine terms will be approximately in phase and only depend weakly on n. Thus, taking the cosine terms to be roughly constant, and independent of n,

$$\langle x \rangle_{-1}^{(1)} \sim \gamma_2 \exp[-\gamma_1^2] \exp[-\gamma_2^2] \sum_{n=1}^{\infty} C(n+1)C(n-1)\sqrt{n(n+1)} \qquad (3.31)$$

and using definitions of $C(n)$, A, and $\exp[\gamma_1^2] = \sum_{n=0}^{\infty} (\gamma_1^2)^n/n!$, we find

$$\langle x \rangle_{-1}^{(1)} \sim \gamma_1^2 \gamma_2 \exp[-\gamma_2^2] \sim \gamma_1^2 \gamma_2 \sim d_1^2 d_2. \qquad (3.32)$$

Note that we ignore any dependence on d_1 contained in the cosine terms (arising from dependence on $\bar{n}$ of the expansion of $\omega_{n+1} - \omega_n$, which in turn is related to d_1). Figure 3.5 plots the amplitude of the pre-revival echo as a function of $d_1^2 d_2$. Note that echo amplitude appears to scale linearly with $d_1^2 d_2$. For comparison, in

the inset we plot the amplitude as a function of d_2, where lines connect simulations with equal values of d_1.
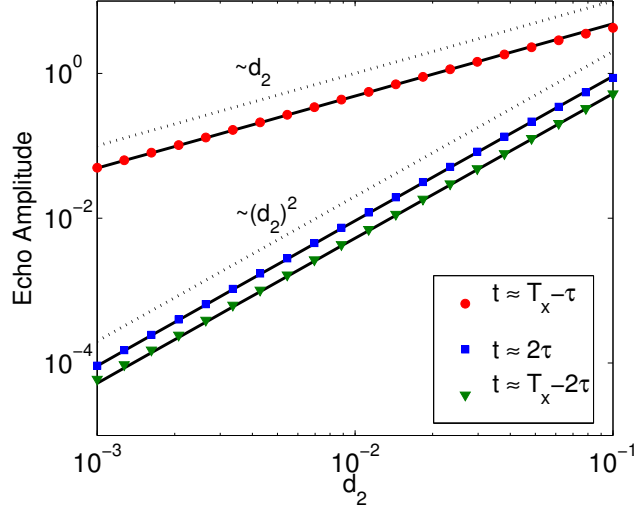
Figure 3.4: The amplitude of three echoes present at different times as a function of d_2 for $d_1 = 5$, $\beta = 0.001$, $\tau = 1899$, ($t \approx T_x - \tau$: circles, $t \approx T_x - 2\tau$: squares, $t \approx 2\tau$: triangles). The solid lines are echo response amplitudes extracted from the perturbation theory model. The dotted lines are guides to the eye indicating linear and quadratic behavior. We note that the pre-revival echo at $t \approx T_x - \tau$ scales linearly with d_2, while the echo responses at $t \approx 2\tau$ and $t \approx T_x - 2\tau$ scale quadratically.

A similar procedure can be implemented for the response at $t \approx \tau$, and the echoes at $t \approx T_x + \tau$, $t \approx 2\tau$ and $t \approx T_x \pm 2\tau$. The response at $t \approx \tau$ and the revival echo at $t \approx T_x + \tau$ are given by Eq. (3.28). Summing over the coefficient gives

$$\langle x \rangle_1^{(1)} \sim d_2 \tag{3.33}$$

44

with approximately no d_1 dependence, which we numerically verify but do not show. For the echo at $t \approx 2\tau$ and the revival echoes at $t \approx T_x \pm 2\tau$, the oscillatory terms in Eqs. (D.3) and (D.4) are assumed to be in phase, and the summations are done over the coefficients, leading to

$$\langle x \rangle_2^{(2)} \sim d_1^3 d_2^2 + \mathcal{O}(d_1 d_2^2) \tag{3.34}$$

$$\langle x \rangle_{-2}^{(2)} \sim d_1^3 d_2^2 \tag{3.35}$$

Thus we expect the echoes and revival echoes to approximately scale as $d_1^3 d_2^2$. Figure 3.6, which plots the echo amplitudes as functions of $d_1^3 d_2^2$, for $\beta = 0.001$, $3.5 \leq d_1 \leq 6$ and $0.001 \leq d_2 \leq 0.07$ and $\tau = 1699$, confirms this expectation. (The post-revival echo at $t \approx T_x + 2\tau$ is the recurrence of the echo at $t \approx 2\tau$. It has an amplitude very similar to the $t \approx 2\tau$ echo and is not shown in Fig. 3.6 for clarity.)

Increasing d_2 to be ~ 1 (where we no longer expect our perturbative model to be valid), Fig. 3.7 plots the values of $\langle x(t) \rangle$ for $\beta = 0.001$, $\tau = 1499$, $d_1 = 5$, and different values of d_2 ranging from $d_2 = 0.1$ to $d_2 = 0.5$. As d_2 is increased, we see that the amplitude of the quantum recurrence at $t \approx T_x$ diminishes. Further, the amplitude of the pre-revival echo at $t \approx T_x - \tau$ is also suppressed, while the amplitude of $\langle x(t) \rangle$ increases for shorter times.

Finally, we note that from numerical experiments solving the Schrödinger equation, at larger d_1 we clearly see an echo at $t \approx 3\tau$ and revival echo at $t \approx T_x - 3\tau$. An example illustrating this is shown in Fig. 3.8.
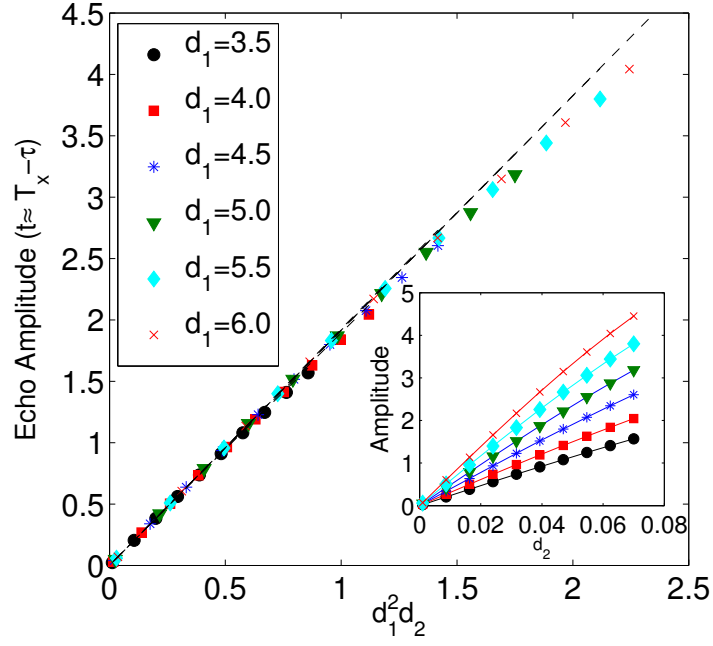
Figure 3.5: The amplitude of the pre-revival echo at $t \approx T_x - \tau$ as a function of $d_1^2 d_2$ for $\beta = 0.001$, $\tau = 2499$, and various values of d_1 ($d_1 = 3.5$: circles, $d_1 = 4.0$: squares, $d_1 = 4.5$: asterisks, $d_1 = 5.0$: triangles, $d_1 = 5.5$: stars, $d_1 = 6.0$: x's). d_2 is allowed to vary between $0.001 \leq d_2 \leq 0.07$. The dotted lines are echo amplitudes extracted from the model equations. We note that the pre-revival echo at $t \approx T_x - \tau$ scales linearly with $d_1^2 d_2$. **(Inset):** The amplitude of the revival echo as a function of d_2, where lines link simulations done at equal values of d_1.
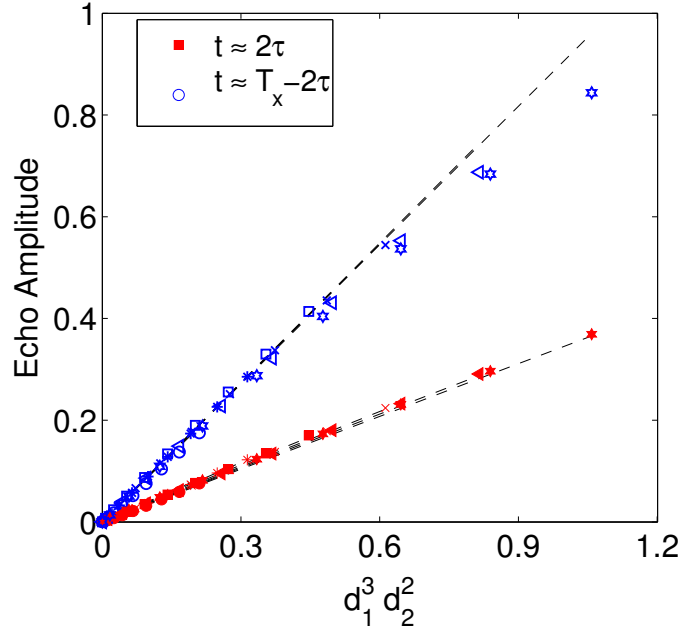
Figure 3.6: The amplitude of the echo at $t \approx 2\tau$ (red, solid) and the pre-revival echo at $t \approx T_x - 2\tau$ (blue, unfilled) as a function of $d_1^3 d_2^2$ for, $\beta = 0.001$, $\tau = 1699$, and various values of d_1 and d_2. $3.5 \leq d_1 \leq 6$ and $0.001 \leq d_2 \leq 0.07$. The dotted lines are echo amplitudes extracted from the model equations. We note that the $t \approx 2\tau$ echo and the pre-revival echo at $t \approx T_x - 2\tau$ scale linearly with $d_1^3 d_2^2$.
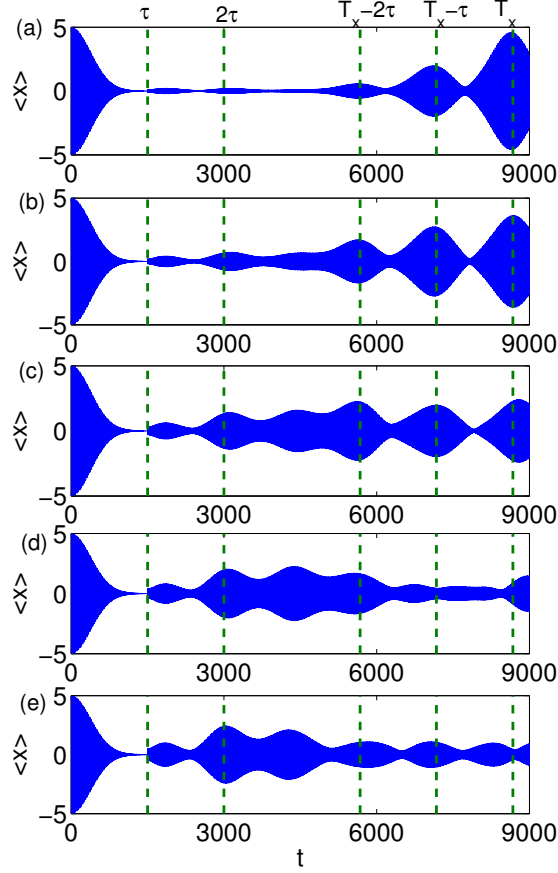
Figure 3.7: $\langle x(t) \rangle$ for $\beta = 0.001$, $\tau = 1499$, $d_1 = 5$, and different values of d_2, **(a)** $d_2 = 0.1$, **(b)** $d_2 = 0.2$, **(c)** $d_2 = 0.3$, **(d)** $d_2 = 0.4$, and **(e)** $d_2 = 0.5$. Note that both the quantum recurrence at $t \approx T_x$ and the pre-revival echo at $t \approx T_x - \tau$ are suppressed as d_2 increases. Further, the amplitude of $\langle x(t) \rangle$ is larger for shorter times as d_2 increases.

Figure 3.8: **(a) and (b):** $\langle x(t) \rangle$ sovled numerically for the full Schrödinger equation for $\beta = 0.001$, $d_1 = 8$, $d_2 = 0.05$ and $\tau = 1299$. Note that an echo at $t \approx 3\tau$ and pre-revival echo $t \approx T_x - 3\tau$ are clearly evident. (b) is the same as (a), plotted on a different scale to better display the echoes.

3.4 Dependence on the Symmetry of the External Perturbations

In Sec. 3.3 we considered echoes and revival echoes induced by two successive displacements of a the trapping potential by amounts d_1 and d_2. For d_2 small, we found that the revival echoes at $t \approx mT_x \pm \tau$ can be much larger (i.e., $\mathcal{O}(d_2)$ as opposed to $\mathcal{O}(d_2^2)$) than the first ordinary echo (i.e., the echo occurring at $t \approx 2\tau$). A possibly significant point is that for small displacement d and symmetric traps, $V(x) = V(-x)$, the perturbation may be viewed as being antisymmetric: $V(x + d) - V(x) = d(dV/dx) + \mathcal{O}(d^2)$. Thus, a natural question is whether our result for the relative sizes of the $t \approx 2\tau$ echo and the revival echoes at $t \approx mT_x \pm \tau$ depend on the symmetry of the stimuli. In what follows we consider this question and show that the answer is affirmative.

We have considered a different type of perturbation at $t = \tau$ which is symmetric in x, an impulse squeeze, i.e., we add a term $\alpha_2 x^2 \delta(t - \tau)$ to the potential. Taking $\beta = 0.001$ and $\tau = 1299$, we numerically calculate the response to an initial shift ($d_1 = 5$) and a small impulse squeeze ($\alpha_2 = 0.005$). We display the results in Fig. 3.9. In this case, echoes and revival echoes are evident in $\langle x(t) \rangle$, at $t \approx 2\tau$ and $t \approx T_x - 2\tau$, with no responses in $\langle x(t) \rangle$ at $t = \tau$ and $t \approx T_x - \tau$. Model expressions for the echoes can be found in the same manner as in Sec. 3.3, and predict that the $t \approx 2\tau$ echo and $t \approx T_x - 2\tau$ revival echo both scale linearly with α_2 (see Appendix D.2). Figure 3.10 plots the amplitude of the echo as a function of α_2, demonstrating that the echo amplitudes depend linearly on α_2. This behavior is due to the impulse squeeze only exciting states of like parity; e.g., the impulse squeeze acting on an

even eigenstate only excites the other even eigenstates. Note that unlike our result in Sec. 3.3, the first $\langle x(t) \rangle$ echo (i.e., at $t \approx 2\tau$) and the first revival echo (i.e., that at $t \approx T_x - 2\tau$) both scale linearly with the strength α_2 of the second perturbation. (In fact it can be shown that all revival echoes at $t \approx mT_x \pm 2\tau$ scale linearly with α_2.)
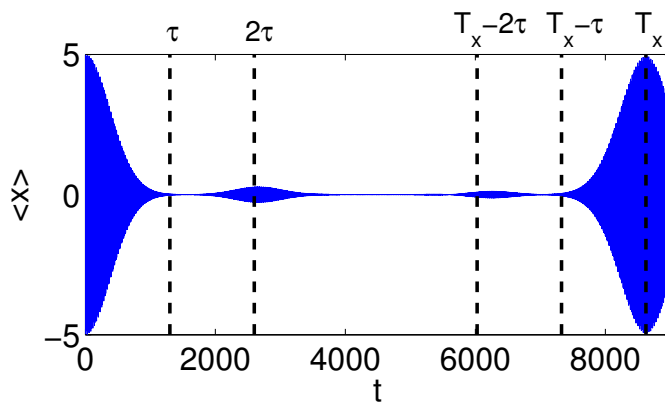
Figure 3.9: $\langle x(t) \rangle$ solved numerically for the full Schrödinger equation with a displacement at t=0 ($d_1 = 5$), and an impulse squeeze at $t = \tau = 1299$ ($\alpha_2 = 0.005$). Notice there is no response at $t = \tau$ or a pre-revival echo at $t \approx T_x - \tau$. An echo at $t \approx 2\tau$ and a pre-revival echo at $t \approx T_x - 2\tau$ are evident and are comparable in size.
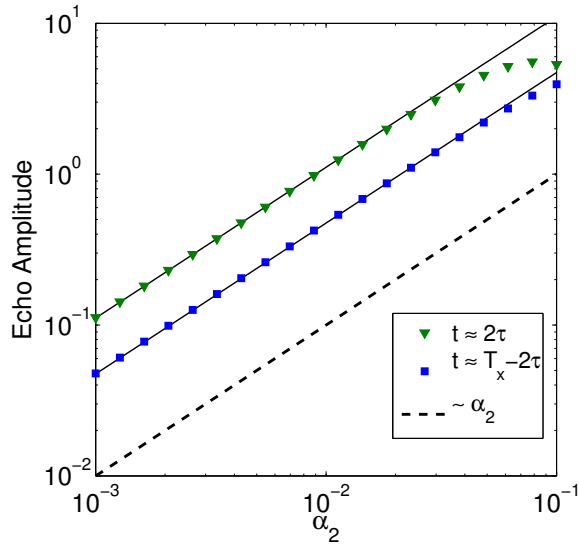
Figure 3.10: The amplitude of the echo at $t \approx 2\tau$ (triangles) and the pre-revival echo at $t \approx T_x - 2\tau$ (squares) as a function of α_2 for, $d_1 = 5$, $\beta = 0.001$, $\tau = 1299$, and various values of α_2. The dotted line is a guide to the eye indicating linear behavior. We note that both echoes scale linearly with α_2. The solid lines are echo amplitudes extracted from a perturbation theory model (see Appendix D.2).

3.5 Quantum Recurrences and Revival Echoes in $\langle x^p(t) \rangle$

Returning to the response to two successive displacements (as in Sec. 3.3), we now examine the behavior of the revival and the revival echoes in the response of $\langle x^p(t) \rangle$, for $p \geq 1$. For example, if one were to measure the width of the cloud of cold atoms, the necessary observable would be $w^2(t) = \langle x^2(t) \rangle - \langle x(t) \rangle^2$. Performing an analysis analogous to that of Sec. 3.3 (described in detail in Appendix D.3), we find that quantum recurrences (in the absence of the second perturbation) are to be expected at fractional times of $t = T_x$. In particular, for the observable $\langle x^p(t) \rangle$, recurrences are expected at times $t \approx mT_x/j$ with $m \geq 1$. The values of j are contingent on whether p is even or odd; for p even: $j = 2, 4, \ldots, p$, and for p odd: $j = 1, 3, \ldots, p$. The amplitude of the recurrences is smaller for larger values of j.

Additionally, revival echoes are also present in $\langle x^p(t) \rangle$. The dominant echoes (those that scale as d_2), are also described by our model in Appendix D.3. Pre-revival echoes are expected at $t \approx (mT_x - \tau)/j$ and post-revivals at $t \approx (mT_x + \tau)/j$, where again $m \geq 1$ and the possible values of j are different for even and odd p; for p even: $j = 2, 4, \ldots, p$, and for p odd: $j = 1, 3, \ldots, p$. For example, for $p = 3$, recurrences are expected at $t \approx mT_x/3$, as well as larger revivals at $t \approx mT_x$, $m \geq 1$. Additionally there are dominant pre and post-revival echoes at $t \approx (mT_x \pm \tau)/3$ and $t \approx mT_x \pm \tau$, for $m \geq 1$. The model suggests that echoes at $t \approx n\tau/j$, $(t \geq \tau)$, and revival echoes at $t \approx (mT_x \pm n\tau)/j$ will scale as γ_2^n.

Figures 3.11(a) and 3.12(a) display the values of $\langle x^p(t) \rangle$ calculated by solving the Schrödinger equation, for $p = 2$, and $p = 3$ after an initial shift perturbation,

$d_1 = 5$, at $t = 0$, and a second shift perturbation, $d_2 = 0.05$, at $t = \tau = 1499$, with $\beta = 0.001$. Displayed in solid lines are the expected times of the quantum recurrences, and in dashed lines, the expected times of the pre and post-revival echoes. For $p = 2$, echoes at $t \approx 3\tau/2$ and $t \approx 4\tau/2$ are expected to be very small, scaling as $(d_2)^3$ and $(d_2)^4$, and are not readily evident upon examination of Figure 3.11(a). Regarding the scaling, as for the $p = 1$ case, we note that the scaling of very small echoes may be affected by revivals and echoes occurring due to corrections in the energy eigenstates.

In Fig 3.12, the pre-revival at $t \approx T_x - \tau/3$ is not visible because of the large quantum recurrence at $t \approx T_x$. A conventional echo is expected at $t \approx 2\tau$, scaling as $(d_2)^2$ but is obscured by the revival at $t \approx T_x/3$. For larger values of d_2, and shorter values of τ, we have numerically observed the $t \approx 2\tau$ echo.

Using the model expressions described in Appendix D.3, we compare the numerically calculated values of $\langle x^2(t) \rangle$ and $\langle x^3(t) \rangle$ to those obtained from our model, as shown in Figs. 3.11(b) and 3.12(b). Note that there is good agreement between the numerics and the model. In both the $\langle x^2(t) \rangle$ and $\langle x^3(t) \rangle$ cases, the response is dominated by the quantum recurrences, and the pre and post-*revival* echoes.
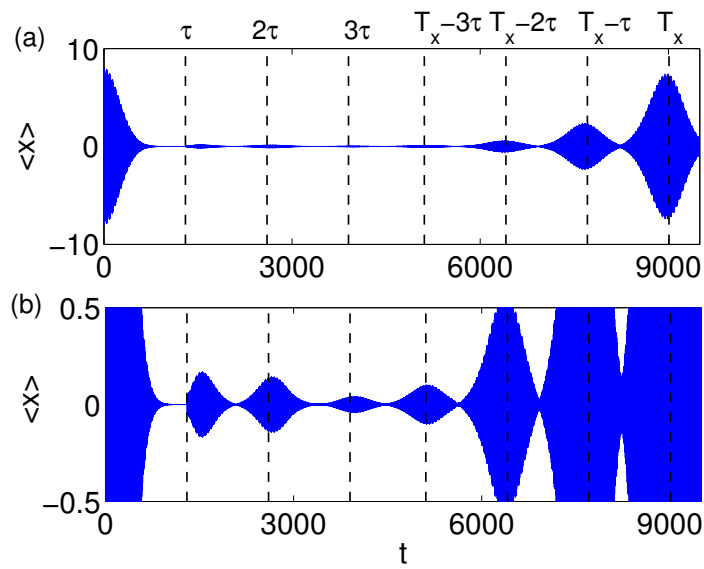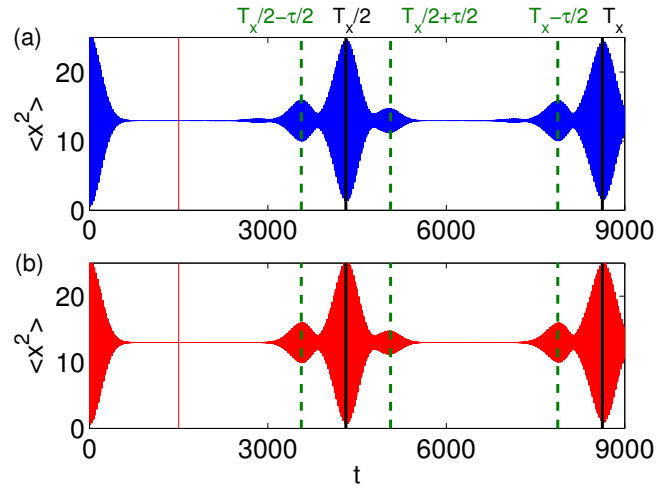
Figure 3.11: **(a) and (b):** $\langle x^2(t) \rangle$ sovled numerically for the full Schrödinger equation for $\beta = 0.001$, $d_1 = 5$, $d_2 = 0.05$ and $\tau = 1499$. Note that recurrences are present at $t \approx T_x$ and $t \approx T_x/2$ (solid lines). Also, pre-revival echoes at $t \approx (mT_x - \tau)/2$, $m = 1, 2$ and a post revival echo $t \approx (T_x + \tau)/2$ are evident (dotted lines). (b) The value of $\langle x^2(t) \rangle$ calculated using the model in Appendix D.3.
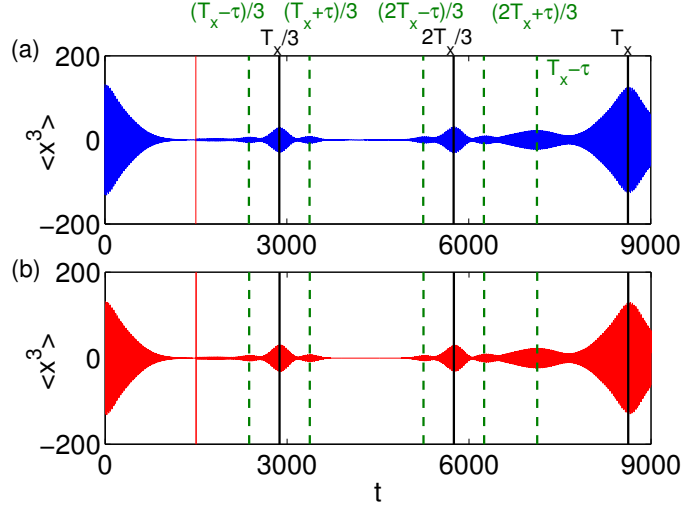
Figure 3.12: **(a) and (b):** $\langle x^3(t) \rangle$ sovled numerically for the full Schrödinger equation for $\beta = 0.001$, $d_1 = 5$, $d_2 = 0.05$ and $\tau = 1499$. Note that recurrences are present at $t \approx T_x$ and $t \approx mT_x/3$, $m = 1, 2$ (solid lines). Also, pre-revival echoes can be seen at $t \approx (mT_x - \tau)/3$, $m = 1, 2$ as well as $t \approx T_x - \tau$. Post revival echoes are evident at $t \approx (mT_x + \tau)/3$,$m = 1, 2$ (dotted lines). (b) The value of $\langle x^3(t) \rangle$ calculated using the model in Appendix D.3.

3.6 Atom-atom Interactions

Finally, we include a cubic nonlinear term in the Hamiltonian and numerically solve for the wavefunction. This can be considered as the mean field approximation for the condensate wavefunction of a Bose-Einstein condensate with interactions, and is known as the Gross-Pitaevskii equation (GPE) [15, 64, 65].

$$i\frac{\partial}{\partial t}\psi = (H_0 + H_1 + H_{int})\psi \tag{3.36}$$

$$H_{int} = u|\psi|^2.$$

Here u is a nonlinear interaction strength, which quantifies repulsive ($u > 0$) or attractive ($u < 0$) interactions in the condensate. Again considering echo responses to two successive displacement (as in Sec. 3.3) and taking $d_1 = 5, d_2 = 0.05$, $\tau = 2499$, and $\beta = 0.001$ for various values of u, we numerically investigate the behavior of the echoes and revival echoes. The results are plotted in Fig. 3.13. As the interaction strength is increased, we note that the damping immediately after $t = 0$ is increased, as compared to the $u = 0$ case. Additionally, for larger values of u, the value of $\langle x(t) \rangle$ does not fully damp away before the application of the second displacement. This observation has been made previously for similar systems [20]. The inclusion of interactions also suppresses the quantum recurrence at $t \sim T_x$, as well as the amplitude of the revival echo at $t \sim T_x - \tau$. The time at which the quantum recurrence occurs is also shifted from the predicted value of $t \approx T_x$ in the noninteracting case.
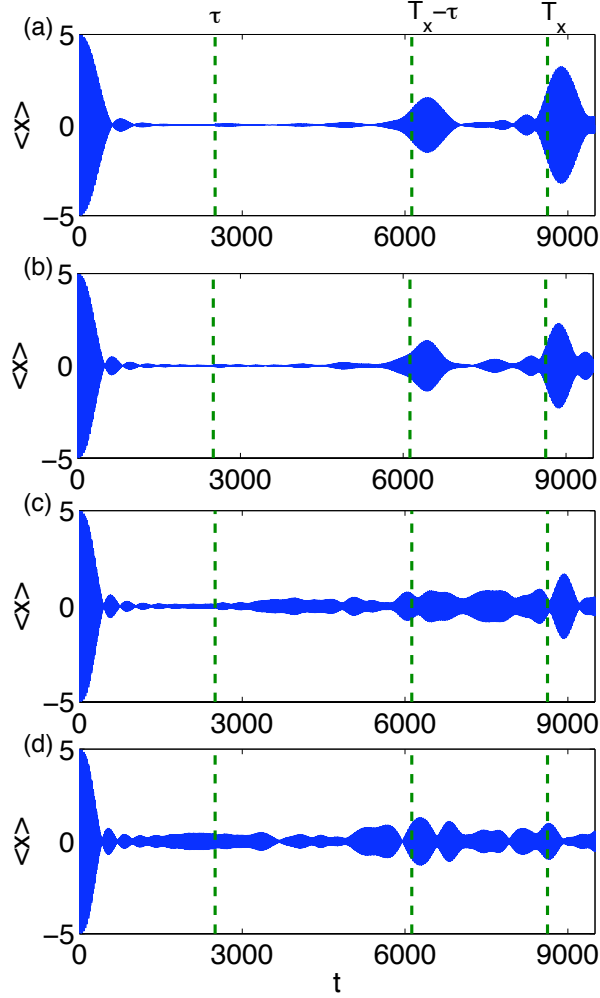
Figure 3.13: The value of $\langle x(t) \rangle$ as a function of time with $d_1 = 5, d_2 = 0.05$, $\beta = 0.001$, $\tau = 2499$, for various values of u. **(a)** $u = 0.05$, **(b)** $u = 0.10$, **(c)** $u = 0.15$, **(d)** $u = 0.20$. We note that while increasing interactions causes damping to occur faster, it also leads to nonzero values of $\langle x(t) \rangle$ before the second kick at $t = \tau$. Further, as u is increased, both the quantum recurrence $t \approx T_x$ and the pre-revival echo at $t \approx T_x - \tau$ are suppressed.

3.7   Summary and Conclusions

In this chapter, we study echoes and revival echoes for a collection of cold atoms in a weakly anharmonic potential subjected to two external stimuli, one at $t = 0$ and the other at $t = \tau$. In the case where the two external stimuli are sudden displacements of sizes d_1 at $t = 0$ and d_2 at $t = \tau$, we observe responses in the expected value of position $\langle x \rangle$, and find that responses occur not only at $t \approx n\tau$, $(n \geq 1)$ and at well-known quantum recurrences at $t = mT_x$, but also at $t \approx mT_x - n\tau > \tau$ (pre-revival echoes) and $t \approx mT_x + n\tau$ (post-revival echoes). Again, in the case where the external stimuli are sudden displacements, we have formulated a perturbation theory model and note good agreement between our model and the numerical results. We numerically verify that for small d_2, the revival echo at $t \approx T_x \pm \tau$ scale linearly with d_2 while echoes at $t \approx 2\tau$ and revival echoes at $t \approx T_x \pm 2\tau$ scale as $(d_2)^2$. As expected from our perturbative model, and seen numerically, this scaling suggests that, for a sufficiently small d_2, the revival echoes at $t \approx T_x \pm \tau$ can be substantially larger than the echo at $t \approx 2\tau$. In addition, our perturbation theory model shows that for small d_1 and d_2, the revival echo at $t \approx T_x - \tau$ scales as $d_1^2 d_2$, (which we numerically verify), while the echo at $t \approx 2\tau$ and the revival echoes at $t \approx T_x \pm 2\tau$ scale as $d_1^3 d_2^2$ (which we numerically verify).

We numerically demonstrate the suppression of the quantum revival $t = T_x$ and the revival echo at $t \approx T_x - \tau$, when the size of the second displacement is increased, $d_2 \sim 1$. We also investigate how the echoes and revival echoes depend on the form and symmetry of the external stimuli. One result is that, in the case

where the first stimuli is a displacement, the domination of the size of the revival echoes at $t \approx mT_x \pm \tau$ over the echoes at $t \approx 2\tau$ does not occur when the small second external stimulus has different symmetry than that of a small displacement.

The presence of quantum recurrences and revival echoes in responses observed in higher moments of position x^p was also studied. Quantum recurrences of $\langle x^p(t) \rangle$ appear at fractions of the $p = 1$ revival time, $t \approx mT_x/j$, where $m = 1, 2, \ldots$, and the value of j is determined by p. Revival echoes are also present in x^p, with dominant echoes (scaling as d_2) at $\langle x^p(t) \rangle$ at times $t \approx (mT_x \pm \tau)/j$.

Finally, the the inclusion of interactions, modeled with the Gross-Pitaevskii equation, demonstrates that the quantum recurrence and the revival echoes are suppressed as the nonlinear interaction strength u, is increased.

Imaging is the natural way to resolve revivals of x. Revivals and echoes in momentum, p, may be found by a similar calculation. In this case, these revivals and echoes may be observed if the trap is switched off at a revival or echo time. The cloud of atoms will move together since all atoms have nearly the same momentum. If instead, the trap is turned off at a time not coinciding with a revival or echo, the cloud of atoms will simply spread.

Chapter 4

Dynamic Localization of a Weakly Interacting Bose-Einstein Condensate in an Anharmonic Potential

4.1 Abstract

We investigate the effect of anharmonicity and interactions on the dynamics of an initially Gaussian wavepacket in a weakly anharmonic potential. We note that depending on the strength and sign of interactions and anharmonicity, the quantum state can be either localized or delocalized in the potential. We formulate a classical model of this phenomenon and compare it to quantum simulations done for a self consistent potential given by the Gross-Pitaevskii equation.

4.2 Introduction

Atoms inside anharmonic traps display a variety of phenomena including wavepacket spreading due to dephasing, and quantum revivals [55, 62]. Additionally, system behavior is also strongly influenced by particle-particle interactions: for

61

example, theoretical [66] and experimental [67] studies have demonstrated that interactions alter the frequency of collective modes of a Bose-Einstein Condensate (BEC). Recently, systems with both anharmonicity and interactions have been studied. The effects of interactions and anharmonicity on the stability of stationary states [68,69], collective motion [19,70–72] and dynamics of coherent states [20] of BECs have been investigated analytically and numerically. Additionally, experimental work has also studied the dynamics of BECs in the presence of anharmonicity [73–75].

Here we consider the quantum evolution of an initially Gaussian wavepacket in a one-dimensional trap with both interactions and anharmonicity, using the description

$$i\frac{\partial}{\partial t}\psi = \left(-\frac{1}{2}\frac{\partial^2}{\partial x^2} + \frac{x^2}{2} + V_a + V_{int}\right)\psi \tag{4.1}$$

where $V_a = \beta x^4/4$, and $V_{int} = u|\psi|^2$. This can be considered as the mean field approximation for the condensate wavefunction $\psi(x,t)$ of a BEC with interactions, and is known as the Gross-Pitaevskii (GP) Equation [15,64,65]. Here β quantifies the anharmonicity of the trap, and u is a nonlinear interaction strength, which quantifies repulsive $(u > 0)$ or attractive $(u < 0)$ interactions. We consider the regime where V_a, V_{int} are smaller than the harmonic oscillator Hamiltonian, and adopt harmonic units, $x = \bar{x}/(\sqrt{\hbar/m\omega_0})$, $t = \omega_0\bar{t}$, where $\bar{x}$ and $\bar{t}$ are the unnormalized units, ω_0 is the frequency of the harmonic oscillator, m is the mass, and the position and momentum operators, x and p satisfy $[x,p] = i$, with the normalization $\int dx|\psi|^2 = 1$. We numerically solve Eq. (4.1) using a split-step Fourier method [17]. One possible experimental realization is the use of a Feshbach resonance [76–79] in order to sample

small repulsive and attractive interaction strengths.

4.3 Numerical Results

Consider an initial, approximately Gaussian wave-packet centered at $x = x_c$, with symmetric widths in x and p, $\Delta_x = \Delta_p = \sqrt{1/2}$. This state may be formed by taking the confined ground state at the center of the potential and discontinuously shifting the potential to the left by an amount x_c. In the case where the potential is formed by the interference of two laser beams, this shift might be accomplished by changing the relative phase of the two beams, for example as in [49].

In the absence of interactions, a wavepacket that overlaps many energy eigenstates of an anharmonic trap will dephase due to the nonuniform spacing of the relevant energy eigenstates. A classical interpretation is that in the phase space, an initial Gaussian distribution subtends various action tori, each with a different frequency. Thus, different parts of the distribution function rotate in the phase space at different rates, leading to spreading of the initial distribution function.

In the presence of interactions, however, we have numerically observed what we term a "dynamical localization" phenomenon in the time evolution of the position density of the wavepacket. For some choices of interaction strength u and anharmonicity β, the wavepacket does not spread over the trap, while for others it does. This is illustrated in Fig. 4.1 where panels (a) to (c) illustrate the position density $|\psi|^2$, obtained from solution of Eq. (4.1), at late times ($t = 1999$) for $\beta = 1.89 \times 10^{-4}$ and three values of interaction strength, one attractive (a) and two repulsive (b and

c). Only in the weakly repulsive case (b) does the wave function spread throughout the trap as it would in the absence of interactions. Figure 4.1(d) displays the value of $\sigma_x \sigma_p$, where σ_x (σ_p) is the standard deviation of position (momentum), averaged from $t = 1899$ to $t = 1999$, for various choices in u and β, and $x_c = -8$. A localized state will have smaller values $\sigma_x \sigma_p$, shown as dark regions while a delocalized state will have larger values, shown as bright regions. The solid (blue) straight lines in Fig. 4.1(d) are results of an approximate theory (given below) for the parameter boundaries separating localized and delocalized behavior. It is important to note that, though one might intuitively expect attractive interactions ($u < 0$) to always lead to localization, Fig. 4.1 demonstrates that this is not so. In fact, for a given value of u, both localized and delocalized behavior is possible, and reversing the sign of both u and β leads to the same behavior.

4.4 Model

To gain insight into the results represented in Fig. 4.1, we introduce a classical model for the dynamical localization effect, which is motivated by our initial choice $|x_c| = 8$, in terms of a classical Hamiltonian. We note for the case of Fig. 4.1, where the state before the shift of the potential is approximated by the ground state of the harmonic oscillator, that, after the shift of the potential, one can show that the state overlaps on the order of $|x_c|$ energy levels. Hence, if $|x_c|$ substantially exceeds one, we expect that a classical treatment will be relevant. Thus we start by considering the classical phase space evolution of the distribution function $f(x, v, t)$

64

of a one-dimensional harmonic oscillator with Hamiltonian $H_0 = p^2/2 + x^2/2$.

Consider the classical Hamiltonian of the harmonic oscillator $H_0 = \frac{1}{2}(p^2 + x^2)$. We introduce as small perturbations an anharmonic potential $V_a = \beta x^4/4$, where β characterizes the strength of the anharmonicity, as well as a self interacting potential $V_{int} = un(x,t)$ where $n(x,t) = \int dv f(x,v,t)$ is the density and u is a parameter describing the interaction strength. The Hamiltonian is then

$$H = H_0 + \epsilon V_a + \epsilon V_{int}. \tag{4.2}$$

Moving to action angle coordinates, the Hamiltonian and equations of motion become:

$$\dot{J} = -\frac{\partial H}{\partial \phi}$$
$$\dot{\theta} = \frac{\partial H}{\partial J}$$
$$H = J + \epsilon \beta J^2 \sin^4(\phi) + \epsilon V_{int}(\sqrt{2J}\sin(\phi), t). \tag{4.3}$$

We do a further change of variables to a rotating frame, $\theta = \phi + \Omega t$ via the generating function $F_2 = J(\theta - \Omega t)$ where Ω is a frequency close to 1, the unperturbed frequency of the harmonic oscillator.

$$\dot{J} = -\frac{\partial H}{\partial \phi}$$
$$\dot{\phi} = \frac{\partial H}{\partial J}$$
$$H = J(1 - \Omega) + \epsilon \beta J^2 \sin^4(\phi + \Omega t) + \epsilon V_{int}(\sqrt{2J}\sin(\phi + \Omega t), t) \tag{4.4}$$

Now we implement a separation of time scales, with a fast time t_0 corresponding to the fast time (the motion of V_{int} in the well), and a slow time $t_1 = \epsilon t$. The chain

65

rule then gives:

$$\frac{d}{dt} \rightarrow \frac{\partial}{\partial t_0} + \epsilon \frac{\partial}{\partial t_1} \tag{4.5}$$

We also expand the action and angle, $J = J_0 + \epsilon J_1$ and $\phi = \phi_0 + \epsilon \phi_1$, as well as

expanding the frequency $\Omega = 1 + \epsilon \delta \Omega$. We can then separate our equations of motion

order by order. The Hamiltonian, separated order by order gives

$$H_0 = 0 \tag{4.6}$$

$$H_1 = -\delta \Omega J_0 + \beta J_0^2 \sin^4(\phi_0 + t_0) + u V_{int}(\sqrt{2J_0} \sin(\phi_0 + t_0), t_0). \tag{4.7}$$

The order (ϵ^0) equations are:

$$\frac{\partial J_0}{\partial t_0} = 0 \tag{4.8}$$

$$\frac{\partial \phi_0}{\partial t_0} = 0 \tag{4.9}$$

$$J_0 = J_0(t_1) \tag{4.10}$$

$$\phi_0 = \phi_0(t_1). \tag{4.11}$$

while the order (ϵ^1) equations are

$$\frac{\partial J_1}{\partial t_0} = -\frac{\partial J_0}{\partial t_1} - \frac{\partial H_1}{\partial \phi_0} \tag{4.12}$$

$$\frac{\partial \phi_1}{\partial t_0} = -\frac{\partial \phi_0}{\partial t_1} + \frac{\partial H_1}{\partial J_0}. \tag{4.13}$$

Note that the right hand sides of Eqs. (4.12) and (4.13) are both periodic on

the short time scales $t_0 = [0, 2\pi]$ and can be interpreted as driving functions for the

first order corrections to J and ϕ. Averaging these equations over a period of the

short time scale, and requiring that $\langle \partial J_1 / \partial t_0 \rangle = \langle \partial \phi_1 / \partial t_0 \rangle = 0$, i.e. the correction

66

terms do not grow secularly as functions of t_0, yields equations for the slow time evolution:

$$\frac{dJ_0}{dt_1} = -\frac{\partial \langle H_1 \rangle}{\partial \phi_0}$$

$$\frac{d\phi_0}{dt_1} = \frac{\partial \langle H_1 \rangle}{\partial J_0}$$

$$\langle H \rangle = \frac{3}{4}\beta J_0 \left(\frac{1}{2}J_0 - J_c\right) + \langle V_{int} \rangle \tag{4.14}$$

where $J_c = x_c^2/2$. The evolution of the slow-time trajectories (or the trajectories averaged over the short period) approximately follow contours of constant $\langle H \rangle$. We have determined the value of $\delta\Omega$ by requiring that $\dot{\phi}|_{J_c} = 0$, since we are in a moving frame such that the center of the distribution function is stationary, and assuming no contribution to the frequency from $\langle V_{int} \rangle$.

In order to average the interaction potential, we are required to average the density over an oscillation period. Recall that the initial phase space distribution is Gaussian in x and p, centered about some $x = x_c$, $p = 0$ with width $\Delta_x = \Delta_p = \Delta = \sqrt{1/2}$. We now evaluate $\langle V_{int} \rangle$ for the early time evolution of the phase space distribution, i.e., when that distribution is still approximately Gaussian. Noting that the Gaussian distribution does not change appreciably over one oscillation period, allows us to average V_{int}, leading to

$$\langle V_{int} \rangle = \frac{u}{2\pi\sqrt{\pi}} \int_0^{2\pi} dt_0 \exp[-(\sqrt{2J}\sin(\phi_0 + t_0)$$

$$- \sqrt{2J_c}\sin(t_0))^2]. \tag{4.15}$$

Numerically calculating the average of the potential, we can then estimate $\langle H \rangle$. Figures 4.2(a)-(d) plot contours of $\langle H \rangle$ in black for different choices of interaction

67

strength u and anharmonicity β, with $J_c = 32$, $|x_c| = 8$.

There is a difference in the nature of the phase space when u and β have opposite signs, Figs. 4.2(a) and (b), and when u and β have the same sign, Figs. 4.2(c) and (d). From Eqs. (4.14) and (4.15), we see that reversing the sign of both u and β leaves phase space unchanged. For u and β of opposite signs, a fixed point is present at $(J, \phi) = (J_c, 0)$, and a separatrix (shown in bold) separates free streaming trajectories from trajectories orbiting the fixed point. In contrast, for u and β of the same sign, while an elliptic point is still present at $(J, \phi) = (J_c, 0)$, additional hyperbolic points typically appear on the $\phi = 0$ axis. A separatrix (bold) again separates trajectories which orbit about the fixed point from those that do not, and, the trajectories immediately outside the separatrix are swept away from the region of the fixed point to values of higher J. Note that the size of the region of confined trajectories increases for larger values of $|u/\beta|$. Plotted in color in Fig. 4.2 are numerically calculated trajectories with V_{int} given by Eq. 4.3. As can be seen, the trajectories have both a short time motion (fast oscillations) and long time motion in the phase space, with the long time motion given approximately by the contours of $\langle H \rangle$.

We interpret the formation of a classical elliptic region around $(J, \phi) = (J_c, 0)$ as arising from a nonlinear resonance [80] between the integrable motion of the anharmonic well and a periodic driving term. This has been studied quantum mechanically, for example, in the rovibrational modes of diatomic molecules [81] and in the dynamics of Rydberg atoms [82, 83]. One important difference, is that in this example, the driving is not due to an external field. Rather, the conden-

sate/wavepacket drives *itself* on resonance because $V_{int} = un(x,t)$. As we discuss below, this feedback between the density and V_{int} can lead to dynamics which can either be localizing or delocalizing.

Figure 4.2 is constructed using a prescribed oscillating Gaussian potential. We now replace it with the self consistent interaction potential $V_{int} = un(x,t)$. The contours of $\langle H \rangle$ found from Eqs. (4.14) and (4.15) will only describe classical trajectories for early times unless the wavefunction retains its localized character. To this end we consider the size of the confining region compared to the extent of the Wigner function (the quantum analog to the phase space distribution, which is equal to the Gaussian distribution function at $t = 0$).

Building upon insight gained from the classical model, it is reasonable to expect that if an initial Wigner function is well confined, that is, enclosed in the classical separatrix denoting orbiting trajectories, the Wigner function will remain localized in the phase space at later times. Similarly, if the Wigner function, is not well confined in the separatrix, then at later times it will become delocalized in the phase space. Qualitatively, as the wavepacket leaves the confining region, the strength of V_{int} decreases. This altering of the potential leads to time dependent behavior with more of the wavepacket leaving the confining region, and coexistence of a delocalized component of the state, and a localized component (most easily seen in the Husimi function representation) at lower values of action.

For example, in Figs. 4.3(a) and 4.3(b) we plot the initial Husimi function $Q(J,\phi)$ (equivalent to the Wigner function smoothed over a Gaussian function in order to assure non-negative values for all times), in the (J, ϕ) coordinates at $t = 0$

69

for various values of u with $\beta = 2 \times 10^{-4}$. Plotted in bold is the classical separatrix from the Gaussian model described previously, for the figures' respective values of u and β; in Fig. 4.3(a) $u = 0.5$ and $\beta = 2 \times 10^{-4}$, while in Fig. 4.3(b) $u = 0.1$ and $\beta = 2 \times 10^{-4}$. We note that in Fig. 4.3(a), the Husimi function is still relatively localized inside the classical separatrix at late times, Fig. 4.3(c). However, in Fig. 4.3(b), where the initial Husimi extends beyond the classical separatrix, the Husimi function it not as well localized inside the classical separatrix at late times Fig. 4.3(d). The quantity F appearing in Figs. 4.3(a) and 4.3(b) is the fraction of the initial Wigner function which lies inside the confining separatrix, and reflects the difference in initial confinement between the two cases.

We test the separatrix expectation numerically by choosing different values of u and β, and calculating the quantum evolution of an initially Gaussian wavepacket centered at $(x, p) = (-8, 0)$. Recall that the classical model demonstrates that the size of the confining region is dependent on the sizes and signs u and β. Using our classical model, we find for given values of u and β the fraction of the initial Wigner function that is contained in the confining separatrix, $F(u, \beta)$. Figure 4.1(d) plots in color (bold lines) contours of $F(u, \beta)$ corresponding to $F = 0.9$. Note that regions yielding poor initial, classical confinement, $F < 0.9$ correspond to delocalized wavepackets at late times, while regions yielding substantial initial confinement, $F > 0.9$, correspond to localized wavepackets at late times. Additionally, we have seen good agreement between localized (delocalized) numerical solutions and well (poorly) confined regions for other values of initial displacement that we have considered, $|x_c| = 6$ and 9.5. It should be noted that this model produces similar behavior

to numerical [20] and experimental [74] results reported previously for $u > 0$ in the strongly interacting regime. While keeping u fixed, as the effect of anharmonicity is increased (in this case by making β more positive, or in the previously reported cases by increasing the value of $|x_c|$), the wavepacket becomes delocalized in the phase space, as seen in Fig. 4.1.

4.5   Conclusion

We note that one of the interesting features of our model is the invariance of the appearance of localization under simultaneous sign changes of u and β. This is reflected in both the numerical results of the GP Equation, Fig. 4.1(d), and the topology of classical phase space, Fig. 4.2. The tendency to form a localized state is strongest when u and β have opposite signs: that is, when the trap oscillation frequency increases with action ($\beta > 0$) and interactions are attractive ($u < 0$), or oscillation frequency decreases with action ($\beta < 0$) and interactions are repulsive ($u > 0$). This latter case is an analog of the "negative mass instability" [84] that leads to bunching of a charged particle beam undergoing circular motion when the angular frequency decreases with energy. Particles leading the bunch are repelled by the bunch, gain energy, lower their rotation rate, and fall back towards the bunch. By this process, a beam with a uniform distribution of rotation phases will spontaneously form a bunch. Likewise, in a trap an initial wave function that is delocalized will spontaneously tend to bunch.

Finally, we note that the interaction values considered here are accessible in

experiments. One possible experimental realization is a lattice of one dimensional "tubes" formed by the interference of multiple lasers [85]. In our units, the required s-wave scattering length a_s is related to the interaction parameter u as $a_s = u\omega_0\delta/(2N\omega_\perp)$, [17], where N is the number of atoms per tube, $\omega_\perp$ is the frequency in the transverse direction, and ground state width $\delta = [\hbar/(m\omega_0)]^{1/2}$. Taking $\omega_\perp/(2\pi) \sim 49$ KHz (which is reasonable with light of wavelength $\lambda = 1064$ nm and the atomic species ^{39}K) $\omega_0/(2\pi) = 2$ KHz, $N = 100$, and $u = 0.5$ leads to $a_s \sim 0.036$ nm. Recently, a group [78, 79] used the Feshbach resonance in ^{39}K to achieve a_s as small as 5.29×10^{-3} nm.
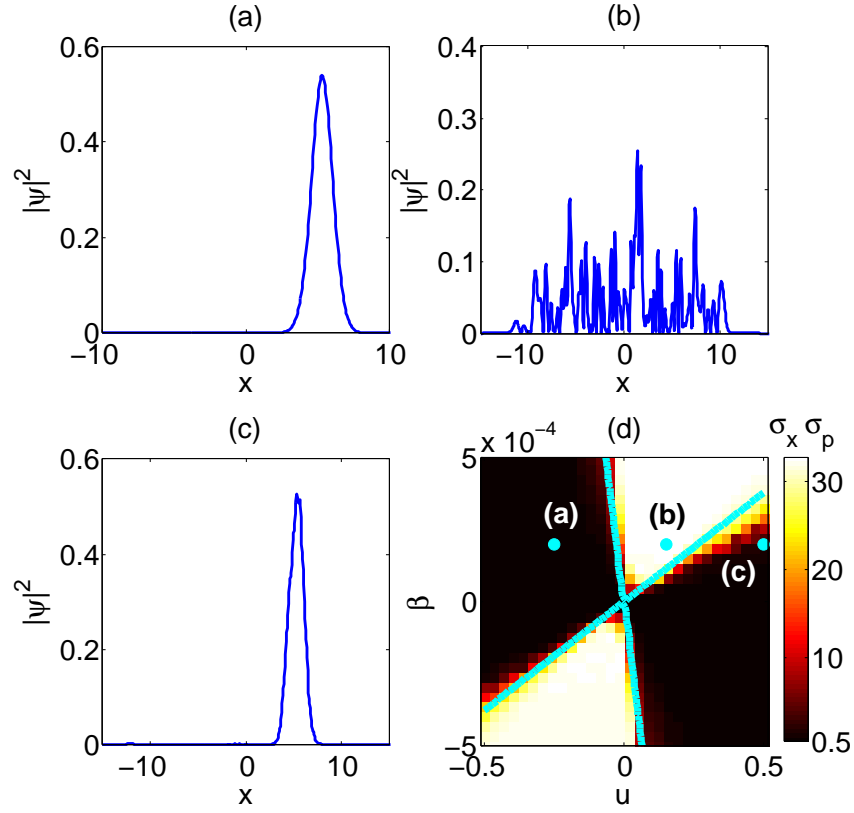
Figure 4.1: (a)-(c): The position density $|\psi|^2$ at $t = 1999$ for $\beta = 1.89 \times 10^{-4}$ with different values of u, (a) $u = -0.2586$, (b) $u = 0.1552$, and (c) $u = 0.50$. Note that increasing repulsive interaction strength can lead to localization. (d): Values of $\sigma_x \sigma_p$ for different values of u and β. Bright regions indicate delocalized behavior (large $\sigma_x \sigma_p$), dark regions indicate localized behavior (small $\sigma_x \sigma_p$). The solid lines (blue) are theoretical predictions separating regions of poor initial confinement and strong initial confinement.
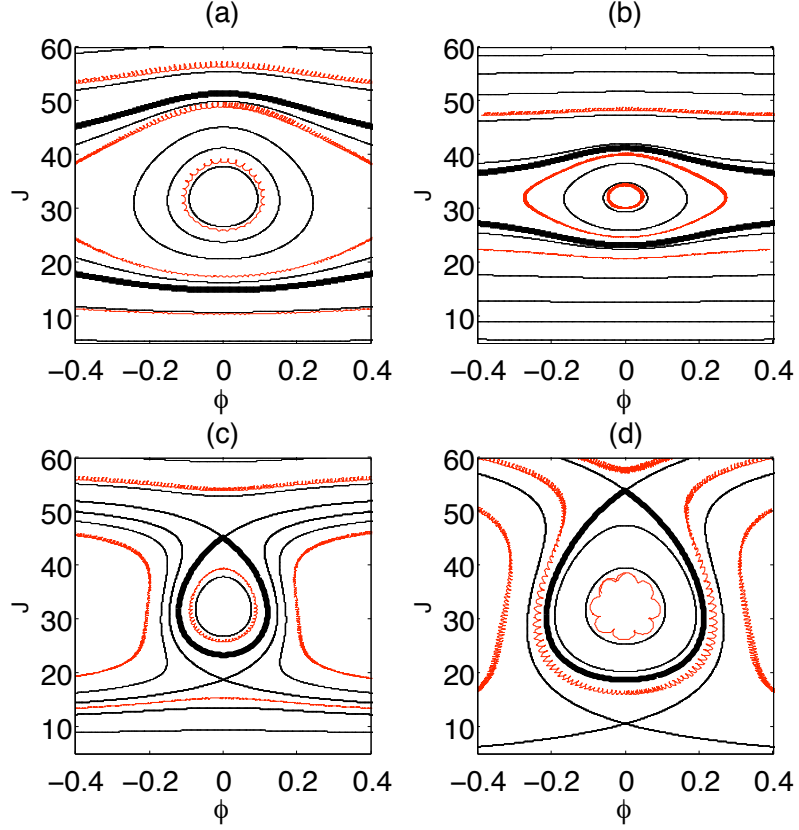
Figure 4.2: Contours of $\langle H \rangle$ (black curves) for various values of interaction strength u (a)=-0.20, (b)=-0.02, (c)=0.10, (d)=0.5 with $\beta = 2 \times 10^{-4}$. Separatrices are shown in bold, separating free streaming and confined trajectories. In red are numerically calculated trajectories under the influence of an external potential of the form in Eq. (4.15). The trajectories consists of short time (fast oscillations) and long time behavior.
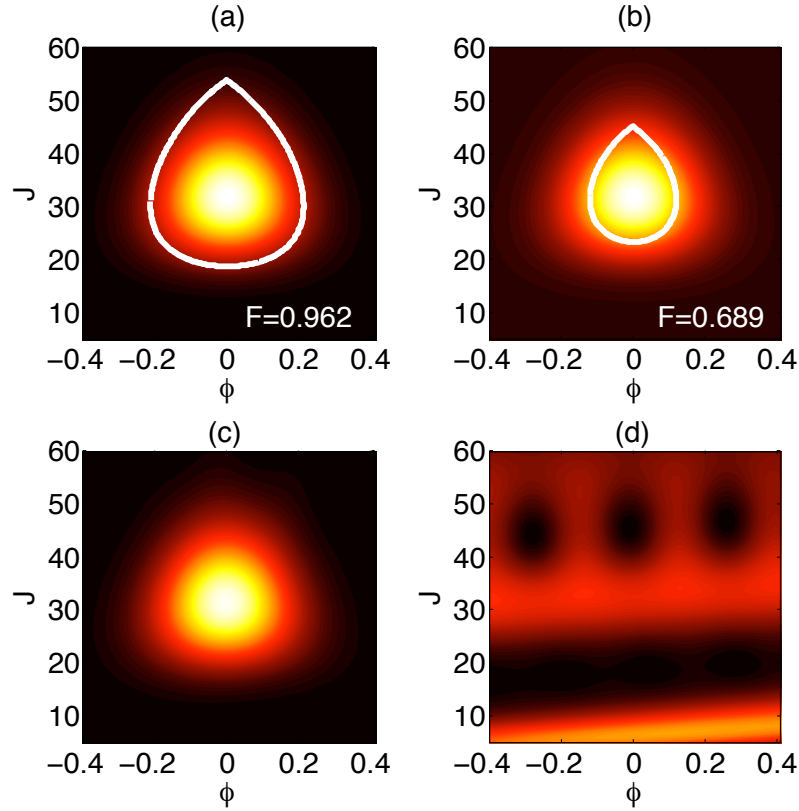
Figure 4.3: The Husimi functions at $t = 0$ (a)-(b) , and at $t = 1999$ (c)-(d) under the influence of the GP equation. In (a) and (b), the classical separatrix from the early time model is plotted in bold. In (a) $u = 0.5$, $\beta = 2 \times 10^{-4}$, the initial condition is well contained inside the classical separatrix found with the early time model . In (b) $u = 0.1$, $\beta = 2 \times 10^{-4}$, however, the initial condition extends well beyond the classical separatrix. (c) demonstrates that the initially well contained wavepacket continues to remain localized at late times, while (d) demonstrates that the poorly contained wavepacket has spread in the potential (color scale narrowed to show detail). (In (c) we have applied a small shift $\Delta\phi = 0.31$ to recenter the Husimi function on $\phi = 0$.)

Appendix A

Nondimensionlisation of GP Equation

Starting with the one-dimensional GP Equation in a weakly anharmonic potential:

$$i\hbar\frac{\partial}{\partial t}\psi = \left(-\frac{\hbar^2}{2m}\frac{\partial^2}{\partial x^2} + \frac{m\omega^2}{2}x^2 + \frac{\beta}{4}x^4 + u|\psi|^2\right)\psi. \tag{A.1}$$

Normalizing the time as $\bar{t} = \omega_0 t$, position $\bar{x} = x/\Delta_0$ where $\Delta_0 = \sqrt{\hbar/(m\omega_0)}$, and adopting the normalization convention

$$\int d\bar{x}|\bar{\psi}|^2 = 1 \tag{A.2}$$

leads us to normalize the wavefunction $\bar{\psi}(\bar{x}) = (\Delta_0)^{1/2}\psi(x)$. Substituting yields the unitless GP Equation:

$$i\frac{\partial}{\partial \bar{t}}\bar{\psi} = \left(-\frac{1}{2}\frac{\partial^2}{\partial \bar{x}^2} + \frac{1}{2}\bar{x}^2 + \frac{\bar{\beta}}{4}\bar{x}^4 + \bar{u}|\bar{\psi}|^2\right)\bar{\psi}. \tag{A.3}$$

where

$$\bar{\beta} = \frac{\beta\hbar}{m^2\omega_0^3} \tag{A.4}$$

$$\bar{u} = \frac{u}{m\omega_0^2}\left(\frac{m\omega_0}{\hbar}\right)^{3/2}. \tag{A.5}$$

Using the expression for the effective 1D interaction strength in a ciger trap potential,

$$u = 2\hbar N a_s \omega_\perp \tag{A.6}$$

leads to an expression for the unitless interaction strength as

$$\bar{u} = 2Na_s \frac{\omega_\perp}{\omega_0} \sqrt{\frac{m\omega_0}{\hbar}}. \tag{A.7}$$

Appendix B

Wigner and Husimi Functions

The Wigner quasi-distribution function was introduced by Wigner [86,87] as a way to represent a phase space analog to a quantum state. Given a quantum state in the position representation $\psi(x)$, the Wigner function for a pure state is defined as

$$W(x,p) = \frac{1}{2\pi\hbar} \int_{-\infty}^{\infty} ds \ \psi(x+s/2)\psi^*(x-s/2) \exp[-ips/\hbar]. \qquad (B.1)$$

$W(x,p)$ has some properties reminiscent of a classical phase space distribution function. For example, density in x or p is given by the marginal distributions (integration on p or x respectively):

$$|\psi(x)|^2 = \int_{-\infty}^{\infty} dp W(x,p) \qquad (B.2)$$

$$|\phi(p)|^2 = \int_{-\infty}^{\infty} dp W(x,p) \qquad (B.3)$$

$$1 = \int_{-\infty}^{\infty} \int_{-\infty}^{\infty} dx dp W(x,p) \qquad (B.4)$$

Moreover, $W(x,p)$ can be shown to obey a Liouville like equation [17]:

$$\frac{\partial W}{\partial t} = \sum_{s=0}^{\infty} \frac{(-1)^2}{(2s+1)!} \left(\frac{\hbar}{2}\right)^{2s} \frac{\partial^{2s+1}}{\partial x^{2s+1}} H \frac{\partial^{2s+1}}{\partial p^{2s+1}} W - \frac{\partial}{\partial p} H \frac{\partial}{\partial x} W. \qquad (B.5)$$

Setting $\hbar \to 0$ yields the Louiville Equation.

A minimum uncertainty wavepacket $\Delta x = \Delta p = \hbar/2$ centered at x_0, p_0 will

have an equivalent Wigner representation as:

$$W_G(x,p) = \frac{1}{\pi\hbar} \exp\left[-\frac{(x-x_0)^2 + (p-p_0)^2}{\hbar}\right].$$ (B.6)

The interpretation of the Wigner function as a phase space-distribution is problematic, however, because it is not positive semi-definite for all states; i.e. it is not clear how to interpret a negative probability. In order to avoid this problem of negative values, the Husimi function [88,89] $Q(x,p)$ has been introduced as another phase space representation of a quantum state, and is given as

$$Q(x,p) = \frac{1}{2\pi\hbar}|\langle\psi|x,p\rangle|^2$$ (B.7)

where $|x_0,p_0\rangle$ is a coherent state (minimum uncertainty gaussian wavepacket, with $\langle x\rangle = x_0$ and $\langle p\rangle = p_0$. Additionally, the Husimi function can be found by convolving $W(x,p)$ with a 2D Gaussian distribution in the phase space.

Appendix C

Numerical Methods

C.1 Split-Step Method

Let us rewrite the NLSE/GPE as:

$$i\partial\psi(x,t) = (\hat{D} + \hat{N})\psi(x,t) \tag{C.1}$$

$$\hat{D} = -\frac{1}{2}\partial_x^2 \tag{C.2}$$

$$\hat{N} = V(x) + u|\psi|^2 \tag{C.3}$$

$\hat{D}$ is the kinetic energy operator and $\hat{N}$ corresponds to the position dependent nonlinear operator. The split-step method obtains solutions for the NLSE by propagating from t to $t + \Delta t$ in two steps. In the first step, the nonlinear (position) term acts alone and $\hat{D} = 0$, and in the second step, the kinetic energy (momentum) term acts alone and $\hat{N} = 0$. Then, the wavefunction at time $t + \Delta t$ is given as

$$\psi(x, t + \Delta t) \simeq \exp[-i\Delta t \hat{D}] \exp[-i\Delta t \hat{N}]\psi(x,t). \tag{C.4}$$

Here, the propagation due to $\hat{N}$ is done in the position representation. In order to propagate in the momentum representation, the state is first transformed into the momentum representation $\phi(p)$ via a FFT, and then the kinetic energy (which is diagonal in p) is applied. In terms of the FFT operation F the state at $t + \Delta t$ is

given as:

$$\psi(x, t + \Delta t) \simeq F^{-1} \exp[-i\Delta t \hat{D}] F \exp[-i\Delta t \hat{N}]\psi(x, t). \qquad (C.5)$$

The error in this scheme can be estimated via the Campbell-Baker-Hausdorff formula. Suppose that $\hat{N}$ where independent of time. Then the solution of the NLSE would be:

$$\psi(x, t + \Delta t) \exp[-i\Delta t(\hat{D} + \hat{N})]\psi(x, t) \qquad (C.6)$$

The split-step operator ignores the non-commutating nature of $\hat{D}$ and $\hat{N}$, and its error can shown via the Baker-Hausdorff formula to be $\sim (\Delta t)^2$ [90].

An improvement can be made to the accuracy of the split-step via a different splitting procedure:

$$\psi(x, t + \Delta t) \simeq \exp[-i(\Delta t/2)\hat{D}] \exp\left[-i \int_t^{t+\Delta t} dt' N\hat{(t')}\right] \exp[-i(\Delta t/2)\hat{D}]\psi(x, t).$$

$$(C.7)$$

where the integral over $\hat{N}(t)$ is to account for the time dependence of the nonlinear operator. A variety of approaches to approximate the integral have been developed. One approach by Agrawal [90] employs the trapezoid rule to approximate the integral via

$$\int_t^{t+\Delta t} \hat{N}(t') \simeq \frac{\Delta t}{2}\left[\hat{N}(t) + \hat{N}(t + \Delta t)\right]. \qquad (C.8)$$

An iterative approach similar to a predictor corrector method is implemented to evaluate the nonlinear term. $\psi(x, t)$ is used for both $\hat{N}(t + \Delta t)$ and $\hat{N}(t)$, and Eq. (C.7) is used to estimate $\psi(x, t + \Delta t)$, which in turn is used for a new value of $\hat{N}(t + \Delta t)$. Two iterations are generally enough in practice.

An alternate leapfrog method [17, 91] uses the time step evolution operator:

$$\psi(x, t + \Delta t) \simeq \exp[-i(\Delta t/2)\hat{D}] \exp\left[-i\Delta t \hat{N}\right] \exp[-i(\Delta t/2)\hat{D}]\psi(x, t). \qquad \text{(C.9)}$$

This method has been shown to be accurate to $\sim (\Delta t)^3$ [91]. In Eq. (C.9), the wavefunction used in evaluating $\hat{N}$ is the most recently calculated state,

$$\hat{N} = V(x) + u|F^{-1}\exp[-i(\Delta t/2)\hat{D}]F\psi|^2. \qquad \text{(C.10)}$$

In order to compare the leapfrog and iterative method, we consider the largest value of interaction strength u contained in this thesis. Taking $u = 0.5$, $\beta = 5 \times 10^{-4}$, at late times $t = 1999$, we plot in Fig. C.1 $|\psi(x, t = 1999)|^2$ for various values time steps $\Delta T = 1/L$ where $L = 250$ or $L = 500$. Note that there is good agreement between the two numeric integration methods at the various values of L. Moreover, in this thesis we are often interested in time dependent expectation values, for example $\langle x \rangle$ as in Chapter 3, or $\sigma_x \sigma_p$ as in Chapter 4. One expects that small deviations in solutions are made less visible in these expectation values because of averaging over all position or momentum space. Again taking values of u and β from above, we calculate the absolute difference between the time dependent quantities $\langle x \rangle_L$ and $(\sigma_x \sigma_p)_L$, where the subscript L is $1/(\Delta t)$. Indeed, these differences are quite small (compared to the values of the observables except when the observables approach zero) as can be seen in Fig. C.2

Finally, we comment on the validation of our numerical scheme. Using the well known imaginary time method [17], replacing $t \rightarrow -it$ causes the split-step method to seek out the ground state of the GP Equation. The expectation value of the chemical potential (the nonlinear eigenvalue corresponding to energy in the linear

Schrödinger Equation) can then be calculated. Using Ref. [17] for comparison, we have recalculated the ground states, and compared the chemical potential value to those published to good agreement.

Additionally, one can demonstrate that in a harmonic oscillator, the ground state of the GP Equation, when displaced from the center of the trap, will coherently follow the classical trajectory of a particle in this potential [20], i.e. the center of the wavepacket obeys $\ddot{x}_c = -m\omega^2 x_c$. We have verified that our numerical scheme results in ground-states which oscillate coherently in harmonic potentials.
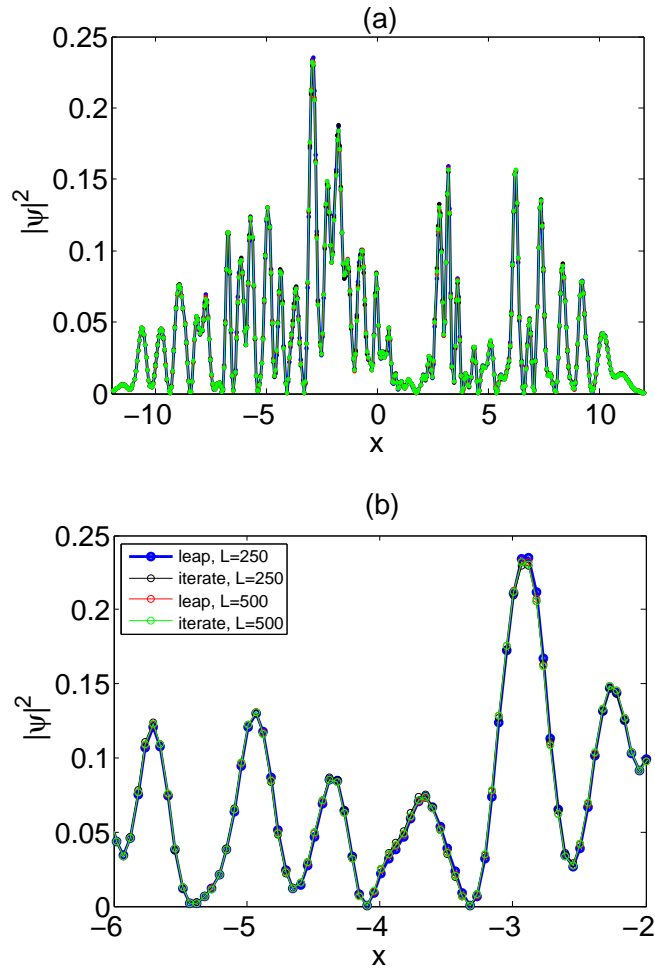
Figure C.1: **(a):** $|\psi|^2$ for $u = 0.5$, $\beta = 5 \times 10^{-4}$, at $t = 1999$, calculated using either the leapfrog or iterative scheme at different values of $dt = 1/L$. **(b):** The same as (a) but zoomed into a smaller range of x for more detail.
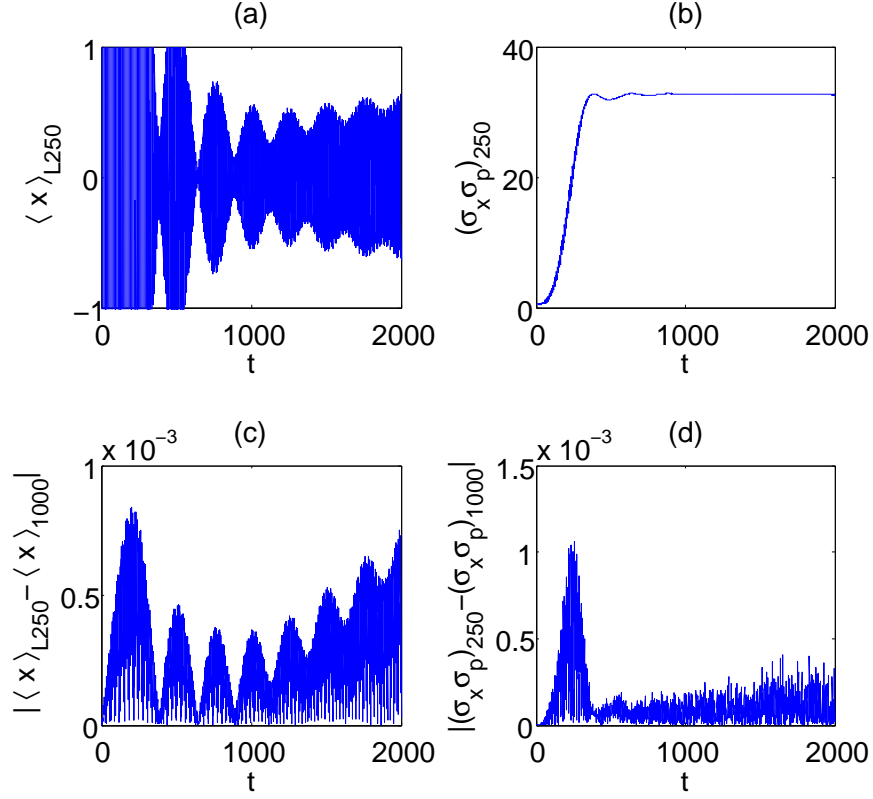
Figure C.2: **(a):** The quantity $\langle x \rangle$ calculated for $u = 0.5$, $\beta = 5 \times 10^{-4}$, and $L = 250$. **(b):** The quantity $\sigma_x \sigma_p$ calculated for the same values. **(c):** The absolute difference between $\langle x \rangle$ calculated at $L = 250$ and $L = 1000$. **(d):** The absolute difference between $\sigma_x \sigma_p$ calculated at $L = 250$ and $L = 1000$. Note that the deviations due to different time time step size are small compared to the late times values of the observables.

Appendix D

Various Model Expressions for Echo Responses

D.1   Expressions for $\langle x \rangle_0^{(2)}$, $\langle x \rangle_2^{(2)}$, and $\langle x \rangle_{-2}^{(2)}$

Continuing the procedure outlined in Sec. 3.3, we can find the terms in the expectation value of $\langle x(t) \rangle$ which are quadratic in γ_2. These can again be separated into the location of their dominant echoes,

$$\langle x(t) \rangle^{(2)} = \langle x \rangle_0^{(2)} + \langle x \rangle_2^{(2)} + \langle x \rangle_{-2}^{(2)}, \tag{D.1}$$

The expressions for $\langle x \rangle_0^{(2)}$, $\langle x \rangle_2^{(2)}$, and $\langle x \rangle_{-2}^{(2)}$ are found to be:

$$\frac{1}{\gamma_2^2} \frac{\langle x \rangle_0^{(2)}}{A^2/\sqrt{2}} = 2 \sum_{n=0}^{\infty} C(n+1)C(n+2)(n+1)\sqrt{n+2}$$

$$\times \cos \left[(\omega_{n+1} - \omega_n)(t - \tau) + (\omega_{n+2} - \omega_{n+1})\tau \right]$$

$$+ 2 \sum_{n=1}^{\infty} C(n-1)C(n)(n+1)\sqrt{n}$$

$$\times \cos \left[(\omega_{n+1} - \omega_n)(t - \tau) + (\omega_n - \omega_{n-1})\tau \right]$$

$$- 2 \sum_{n=0} C(n)C(n+1)(n+1)^{3/2} \cos \left[(\omega_{n+1} - \omega_n)t \right]$$

$$- 2 \sum_{n=2} C(n)C(n-1)\sqrt{n}(n-1) \cos \left[(\omega_n - \omega_{n-1})t \right], \tag{D.2}$$

$$\frac{1}{\gamma_2^2}\frac{\langle x \rangle_2^{(2)}}{A^2/\sqrt{2}} = -2\sum_{n=0} C(n)C(n+1)(n+1)^{3/2}$$

$$\times \cos\Big[(\omega_{n+1}-\omega_n)(t-\tau) + (\omega_n - \omega_{n+1})\tau\Big]$$

$$+\sum_{n=1}^{\infty} C(n)C(n-1)(n+1)\sqrt{n}\cos\Big[(\omega_{n+1}-\omega_n)t + (\omega_{n-1}-\omega_{n+1})\tau\Big]$$

$$+\sum_{n=1}^{\infty} C(n)C(n+1)n\sqrt{n+1}\cos\Big[(\omega_n-\omega_{n-1})t + (\omega_{n-1}-\omega_{n+1})\tau\Big],$$

$$(D.3)$$

and

$$\frac{1}{\gamma_2^2}\frac{\langle x \rangle_{-2}^{(2)}}{A^2/\sqrt{2}} = -2\sum_{n=2}^{\infty} C(n-2)C(n+1)\sqrt{n(n^2-1)}$$

$$\times \cos\Big[(\omega_n-\omega_{n-1})(t-\tau) + (\omega_{n+1}-\omega_{n-2})\tau\Big] \qquad (D.4)$$

$$+\sum_{n=3}^{\infty} C(n)C(n-3)\sqrt{(n)(n-1)(n-2)}$$

$$\times \cos\Big[(\omega_n-\omega_{n-1})t + (\omega_{n-1}-\omega_{n-3})\tau\Big]$$

$$+\sum_{n=0}^{\infty} C(n)C(n+3)\sqrt{(n+1)(n+2)(n+3)}$$

$$\times \cos\Big[(\omega_{n+1}-\omega_n)t + (\omega_{n+3}-\omega_{n+1})\tau\Big].$$

In order to get the approximate scaling for the echo at $t \approx 2\tau$ and the revival echo at $t \approx T_x - \tau$, we take the above expressions for the echoes, and take the cosine terms to be in phase and independent of n. Doing the summations for the

coefficients, we find for $\langle x \rangle_2^{(2)}$:

$$\sum_{n=0}^{\infty} C(n)C(n+1)(n+1)^{3/2} = \exp[\gamma_1^2](\gamma_1^3 + \gamma_1) \tag{D.5}$$

$$\sum_{n=1}^{\infty} C(n)C(n-1)(n+1)\sqrt{n} = \exp[\gamma_1^2](\gamma_1^3 + 2\gamma_1) \tag{D.6}$$

$$\sum_{n=1}^{\infty} C(n)C(n+1)n\sqrt{n+1} = \exp[\gamma_1^2](\gamma_1^3), \tag{D.7}$$

and for $\langle x \rangle_{-2}^{(2)}$:

$$\sum_{n=2}^{\infty} C(n-2)C(n+1)]\sqrt{n(n^2-1)} = \exp[\gamma_1^2](\gamma_1^3) \tag{D.8}$$

$$\sum_{n=3}^{\infty} C(n)C(n-3)\sqrt{n(n-1)(n-2)} = \exp[\gamma_1^2](\gamma_1^3) \tag{D.9}$$

$$\sum_{n=0}^{\infty} C(n)C(n+3)n\sqrt{(n+1)(n+2)(n+3)} = \exp[\gamma_1^2](\gamma_1^3). \tag{D.10}$$

The factor $\exp[\gamma_1^2]$ is canceled by the γ_1 dependence of A^2, leading to the d_1 dependence described in Sec. 3.3.

D.2 Model Expressions for an Initial Displacement, Followed by an Impulse Squeeze.

In a manner analogous to the calculation presented in Sec. 3.3, The response of $\langle x(t) \rangle$ to an initial displacement at $t = 0$ $(d = d_1)$ and an impulse squeeze at time τ $(\alpha = \alpha_2 \,,\, \alpha_2(\bar{n} + 3\sigma_n) \ll 1)$ can also be estimated. Approximating the matrix elements of the squeeze operator in the unperturbed anharmonic oscillator basis, we

find

$$\langle m| \exp[-i\alpha_2 x^2 |n\rangle \approx \delta_{m,n} - i\frac{\alpha_2}{2}\left\{(2n+1)\delta_{m,n} + \sqrt{n(n-1)}\delta_{m,n-2}\right.$$

$$\left. + \sqrt{(n+1)(n+2)}\delta_{m,n+2}\right\}. \tag{D.11}$$

From this, the responses proportional to α_2 can be calculated,

$$\langle x\rangle^{(1)} = \langle x\rangle_2^{(1)} + \langle x\rangle_{-2}^{(1)}$$

where

$$\frac{\langle x\rangle_2^{(1)}}{\exp[-\gamma_1^2]\alpha_2/\sqrt{2}} = \sum_{n=1}^{\infty} C(n)C(n+1)n\sqrt{n+1}$$

$$\times \sin[(\omega_n - \omega_{n-1})t + (\omega_{n-1} - \omega_{n+1})\tau]$$

$$+ \sum_{n=1}^{\infty} C(n)C(n-1)(n+1)\sqrt{n}\sin[((\omega_n - \omega_{n+1})t + (\omega_{n+1} - \omega_{n-1})\tau]$$

$$\tag{D.12}$$

and

$$\frac{\langle x\rangle_{-2}^{(1)}}{\exp[-\gamma_1^2]\alpha_2/\sqrt{2}} = \sum_{n=0}^{\infty} C(n)C(n+3)\sqrt{(n+1)(n+2)(n+3)} \tag{D.13}$$

$$\times \sin[(\omega_n - \omega_{n+1})t + (\omega_{n+1} - \omega_{n+3})\tau]$$

$$+ \sum_{n=3}^{\infty} C(n)C(n-3)\sqrt{n(n-1)(n-2)}$$

$$\times \sin[((\omega_n - \omega_{n-1})t + (\omega_{n-1} - \omega_{n-3})\tau].$$

D.3   Model Expressions for $\langle x^p(t)\rangle$ After Two Shift Perturbations.

In the case of a shift perturbation, d_1, at $t = 0$, and a smaller shift perturbation, d_2, at time $t = \tau$, we derive model equations for both the quantum recurrence,

as well as revival echoes in the quantity

$$\langle x^p(t)\rangle = \langle\psi|x^p|\psi\rangle \tag{D.14}$$

for $p \geq 1$. Using the definition of x in Eq. 3.5, one can write the matrix elements of x^p, in the unperturbed harmonic oscillator basis, as

$$\langle m|x^p|n\rangle = \left(\frac{1}{\sqrt{2}}\right)^p \langle m|(\hat{a} + \hat{a}^\dagger)^p|n\rangle \tag{D.15}$$

$$= \left(\frac{1}{\sqrt{2}}\right)^p \sum_{j=0}^{p} B(n, p - 2j, p)\delta_{m,n+p-2j} \tag{D.16}$$

where $B(n, p - 2j, p)$ are coefficients that can be found via application of the annihilation and creation operators. For example, for $p = 3$, the coefficients are

$$B(n, -3, 3) = \sqrt{n(n - 1)(n - 2)} \tag{D.17}$$

$$B(n, -1, 3) = 3n\sqrt{n} \tag{D.18}$$

$$B(n, 1, 3) = 3(n + 1)\sqrt{n + 1} \tag{D.19}$$

$$B(n, 3, 3) = \sqrt{(n + 1)(n + 2)(n + 3)}. \tag{D.20}$$

It can be shown that these coefficients obey the relation $B(n, -d, p) = B(n - d, d, p)$. Using Eq. (D.16), and the expression for the quantum state after two displacements, Eq. (3.24), one can again find the time dependence of the expectation value of $x^p(t)$, and order the terms according to their dependence on γ_2,

$$\langle x^p(t)\rangle = \langle x^p(t)\rangle^{(0)} + \langle x^p(t)\rangle^{(1)} + \dots \tag{D.21}$$

The term $\langle x^p(t)\rangle^{(0)}$ is again the quantum recurrence in the absence of the second

displacement, and if p is even, is given by,

$$\frac{\langle x^p(t)\rangle^{(0)}}{2A^2(1/\sqrt{2})^p} = \sum_{\substack{j=0 \\ j\text{ even}}}^{p} \sum_{n=0}^{\infty} \left(1 - \frac{\delta_{0,j}}{2}\right) C(n)C(n+j)\cos[(\omega_{n+j} - \omega_n)t]B(n,j,p)$$

(D.22)

and if p is odd,

$$\frac{\langle x^p(t)\rangle^{(0)}}{2A^2(1/\sqrt{2})^p} = \sum_{\substack{j=1 \\ j\text{ odd}}}^{p} \sum_{n=0}^{\infty} C(n)C(n+j)\cos[(\omega_{n+j} - \omega_n)t]B(n,j,p).$$

(D.23)

Employing the same argument for the behavior of the quantum recurrence in Sec. 3.3, one finds

$$(\omega_{n+j} - \omega_n) = (\omega_{n+j} - \omega_{n+j-1}) + (\omega_{n+j-1} - \omega_{n+j-2}) + \cdots + (\omega_{n+1} - \omega_n) \quad \text{(D.24)}$$

$$\approx j\Delta_{\bar{n}} + ja(n - \bar{n} + q).$$

where q is a constant independent of n. Compared to the $j = 1$ case of Sec. 3.3, the slow envelope maxima are now periodic for all n at $2\pi/(ja)$. Thus, each $\cos[(\omega_{n+j} - \omega_n)t]$ will give rise to a recurrence at time

$$t \approx \frac{mT_x}{j}, \quad (j \geq 1, m \geq 1)$$

(D.25)

If p is even, then the $j = 0$ case is a constant which increases the value of $\langle x^p(t)\rangle$. Note that the expectation value of $\langle x^p \rangle$ contains recurrences not only at $t \approx mT_x/p$, but also at the values of $j < p$ as seen in Eqs. (D.22) and (D.23).

The expression for the revival echoes that are approximately linear to d_2 can also be found, for p even:

$$\frac{\langle x^p(t)\rangle^{(1)}}{2\gamma_2(1/\sqrt{2})^p A^2} = \langle x^p \rangle_0^{(1)} + \sum_{\substack{j=2 \\ j\text{ even}}}^{p} \left\{ \langle x^p(t)\rangle_{j+}^{(1)} + \langle x^p(t)\rangle_{j-}^{(1)} \right\}$$

(D.26)

91

and p odd:

$$\frac{\langle x^p(t)\rangle^{(1)}}{2\gamma_2(1/\sqrt{2})^p A^2} = \sum_{\substack{j=1 \\ j\text{ odd}}}^{p} \left\{ \langle x^p(t)\rangle_{j+}^{(1)} + \langle x^p(t)\rangle_{j-}^{(1)} \right\} \tag{D.27}$$

where,

$$\langle x^p\rangle_0^{(1)} = \sum_{n=0}^{\infty} C(n+1)C(n)\sqrt{n+1}\cos[(\omega_{n+1} - \omega_n)\tau][B(n+1,0,p) - B(n,0,p)],$$

$$\tag{D.28}$$

$$\langle x^p(t)\rangle_{j+}^{(1)} = \sum_{n=j}^{\infty} C(n-1)C(n-j)\sqrt{n}B(n,-j,p)$$

$$\times \cos[(\omega_{n-j} - \omega_n)t + (\omega_n - \omega_{n-1})\tau]$$

$$- \sum_{n=0}^{\infty} C(n+1)C(n+j)\sqrt{n+1}B(n,j,p)$$

$$\times \cos[(\omega_{n+j} - \omega_n)t + (\omega_n - \omega_{n+1})\tau], \tag{D.29}$$

and

$$\langle x^p(t)\rangle_{j-}^{(1)} = \sum_{n=1}^{\infty} C(n-1)C(n+j)\sqrt{n}B(n,j,p)$$

$$\times \cos[(\omega_{n+j} - \omega_n)t + (\omega_n - \omega_{n-1})\tau]$$

$$- \sum_{n=j}^{\infty} C(n+1)C(n-j)\sqrt{n+1}B(n,-j,p)$$

$$\times \cos[(\omega_{n-j} - \omega_m)t + (\omega_n - \omega_{n+1})\tau]. \tag{D.30}$$

The term $\langle x^p\rangle_0^{(1)}$ is a time independent offset. The quantity $\langle x^p(t)\rangle_{j+}^{(1)}$ represents a post-revival echo at time $t \approx (mTx + \tau)/j$. Similarly the term $\langle x^p(t)\rangle_{j-}^{(1)}$ gives rise to a pre-revival echo at $t \approx (mT_x - \tau)/j$, $j \geq 1$ and $m \geq 1$. As can be seen from

Eqs. (D.26) and (D.27), revival echoes will be present and at various fractional shifts of τ from the different recurrences. For example, for $p = 3$, recurrences are expected at $t \approx \frac{mT_x}{3}$, as well as larger recurrences at $t \approx mT_x$, $m \geq 1$. Additionally there are dominant pre and post-revival echoes at $t \approx (mT_x \pm \tau)/3$ and $t \approx mT_x \pm \tau$, for $m \geq 1$ (see Figure 3.12).

Bibliography

[1] M. Newman, "The structure and function of complex networks," *SIAM Review*, vol. 45, pp. 167–256, May 2003.

[2] M. Herrera, D. C. Roberts, and N. Gulbahce, "Mapping the evolution of scientific fields," *PLoS ONE*, vol. 5, p. e10355, May 2010.

[3] D. J. de Solla Price, "Networks of scientific papers," *Science*, vol. 149, pp. 510–515, July 1965.

[4] M. E. J. Newman, "Scientific collaboration networks. I. network construction and fundamental results," *Phys. Rev. E*, vol. 64, p. 016131, Jun 2001.

[5] M. E. J. Newman, "Scientific collaboration networks. II. shortest paths, weighted networks, and centrality," *Phys. Rev. E*, vol. 64, p. 016132, Jun 2001.

[6] J. Padgett and C. Ansell, "Robust action and the rise of the Medici, 1400-1434," *American Journal of Sociology*, pp. 1259–1319, May 1993.

[7] N. Zekri and J. P. Clerc, "Statistical and dynamical study of disease propagation in a small world network," *Phys. Rev. E*, vol. 64, p. 056115, Oct 2001.

[8] H. M. Jaeger, S. R. Nagel, and R. P. Behringer, "Granular solids, liquids, and gases," *Rev. Mod. Phys.*, vol. 68, pp. 1259–1273, Oct 1996.

[9] R. Nedderman and C. Laohakul, "The thickness of the shear zone of flowing granular materials," *Powder Technology*, vol. 25, pp. 91–100, Jan 1980.

[10] E. Aharonov and D. Sparks, "Shear profiles and localization in simulations of granular materials," *Phys. Rev. E*, vol. 65, p. 051302, May 2002.

[11] D. M. Mueth, G. F. Debregeas, G. S. Karczmar, P. J. Eng, S. R. Nagel, and H. M. Jaeger, "Signatures of granular microstructure in dense shear flows," *Nature*, vol. 406, pp. 385–389, Jul 2000.

[12] M. Anderson, J. Ensher, M. Matthews, C. Wieman, E. Cornell, *et al.*, "Observation of Bose-Einstein condensation in a dilute atomic vapor," *Science*, vol. 269, pp. 198–201, July 1995.

[13] K. B. Davis, M. O. Mewes, M. R. Andrews, N. J. van Druten, D. S. Durfee, D. M. Kurn, and W. Ketterle, "Bose-Einstein condensation in a gas of sodium atoms," *Phys. Rev. Lett.*, vol. 75, pp. 3969–3973, Nov 1995.

[14] C. C. Bradley, C. A. Sackett, J. J. Tollett, and R. G. Hulet, "Evidence of Bose-Einstein condensation in an atomic gas with attractive interactions," *Phys. Rev. Lett.*, vol. 75, pp. 1687–1690, Aug 1995.

[15] C. J. Pethick and H. Smith, *Bose-Einstein Condensation in Dilute Gases*. Cambridge: Cambridge Univ. Press, 2002.

[16] Y. Castin and R. Dum, "Low-temperature Bose-Einstein condensates in time-dependent traps: Beyond the U(1) symmetry-breaking approach," *Phys. Rev. A*, vol. 57, pp. 3008–3021, Apr 1998.

[17] S. A. Gardiner, D. Jaksch, R. Dum, J. I. Cirac, and P. Zoller, "Nonlinear matter wave dynamics with a chaotic potential," *Phys. Rev. A*, vol. 62, p. 023612, Jul 2000.

[18] N. Bogoliubov, "On the theory of superfluidity," *J. Phys. (USSR)*, vol. 11, no. 23, 1947.

[19] V. M. Pérez-García, H. Michinel, J. I. Cirac, M. Lewenstein, and P. Zoller, "Dynamics of Bose-Einstein condensates: Variational solutions of the Gross-Pitaevskii equations," *Phys. Rev. A*, vol. 56, pp. 1424–1432, Aug 1997.

[20] S. Moulieras, A. G. Monastra, M. Saraceno, and P. Leboeuf, "Wave-packet dynamics in nonlinear Schrödinger equations," *Phys. Rev. A*, vol. 85, p. 013841, Jan 2012.

[21] A. M. Kamchatnov, "Expansion of Bose–Einstein condensates confined in quasi-one-dimensional or quasi-two-dimensional traps," *Zh. Eksp. Teor. Fiz*, vol. 125, p. 1041, May 2004.

[22] T. S. Majmudar and R. P. Behringer, "Contact force measurements and stress-induced anisotropy in granular materials," *Nature*, vol. 435, pp. 1079–1082, Jun 2005.

[23] R. C. Ball and R. Blumenfeld, "Stress field in granular systems: Loop forces and potential formulation," *Phys. Rev. Lett.*, vol. 88, p. 115505, Feb 2002.

[24] K. Vollmayr-Lee and E. A. Baker, "Self-organized criticality below the glass transition," *Euro. Phys. Lett.*, vol. 76, p. 1130, Nov 2006.

[25] D. M. Mueth, H. M. Jaeger, and S. R. Nagel, "Force distribution in a granular medium," *Phys. Rev. E*, vol. 57, pp. 3164–3169, Mar 1998.

[26] R. Arévalo, I. Zuriguel, and D. Maza, "Topology of the force network in the jamming transition of an isotropically compressed granular packing," *Phys. Rev. E*, vol. 81, p. 041302, Apr 2010.

[27] A. Tordesillas, D. M. Walker, and Q. Lin, "Force cycles and force chains," *Phys. Rev. E*, vol. 81, p. 011302, Jan 2010.

[28] D. M. Walker and A. Tordesillas, "Topological evolution in dense granular materials: A complex networks perspective," *International Journal of Solids and Structures*, vol. 47, pp. 624–639, Mar 2010.

[29] M. E. J. Newman and D. J. Watts, "Scaling and percolation in the small-world network model," *Phys. Rev. E*, vol. 60, pp. 7332–7342, Dec 1999.

[30] D. S. Callaway, J. E. Hopcroft, J. M. Kleinberg, M. E. J. Newman, and S. H. Strogatz, "Are randomly grown graphs really random?," *Phys. Rev. E*, vol. 64, p. 041902, Sep 2001.

[31] S. Slotterback, M. Toiya, L. Goff, J. F. Douglas, and W. Losert, "Correlation between particle motion and voronoi-cell-shape fluctuations during the compaction of granular matter," *Phys. Rev. Lett.*, vol. 101, p. 258001, Dec 2008.

[32] J. A. Dijksman, E. Wandersman, S. Slotterback, C. R. Berardi, W. D. Updegraff, M. van Hecke, and W. Losert, "From frictional to viscous behavior: Three-dimensional imaging and rheology of gravitational suspensions," *Phys. Rev. E*, vol. 82, p. 060301, Dec 2010.

[33] W. G. Ellenbroek, E. Somfai, M. van Hecke, and W. van Saarloos, "Critical scaling in linear response of frictionless granular packings near jamming," *Phys. Rev. Lett.*, vol. 97, p. 258001, Dec 2006.

[34] G. Katgert, A. Latka, M. E. Möbius, and M. van Hecke, "Flow in linearly sheared two-dimensional foams: From bubble to bulk scale," *Phys. Rev. E*, vol. 79, p. 066318, Jun 2009.

[35] S. Slotterback, L. Goff, M. Toiya, J. Douglas, M. V. Hecke, and W. Losert, "Microscopic rearrangements in a granular column during compaction by thermal cycling," *AIP Conference Proceedings*, vol. 1145, pp. 489–491, Jul 2009.

[36] J. Saramäki, M. Kivelä, J.-P. Onnela, K. Kaski, and J. Kertész, "Generalizations of the clustering coefficient to weighted complex networks," *Phys. Rev. E*, vol. 75, p. 027105, Feb 2007.

[37] W. Lai, D. Rubin, and E. Krempl, *Introduction to continuum mechanics*. Pergamon Press, 1978.

[38] O. Baran, D. Ertaş, T. C. Halsey, G. S. Grest, and J. B. Lechman, "Velocity correlations in dense gravity-driven granular chute flow," *Phys. Rev. E*, vol. 74, p. 051302, Nov 2006.

[39] C. R. Berardi, K. Barros, J. F. Douglas, and W. Losert, "Direct observation of stringlike collective motion in a two-dimensional driven granular fluid," *Phys. Rev. E*, vol. 81, p. 041301, Apr 2010.

[40] E. L. Hahn, "Spin echoes," *Phys. Rev.*, vol. 80, pp. 580–594, Nov 1950.

[41] E. Ott, J. H. Platig, T. M. Antonsen, and M. Girvan, "Echo phenomena in large systems of coupled oscillators," *Chaos: An Interdisciplinary Journal of Nonlinear Science*, vol. 18, p. 037115, Sep 2008.

[42] R. W. Gould, T. M. O'Neil, and J. H. Malmberg, "Plasma wave echo," *Phys. Rev. Lett.*, vol. 19, pp. 219–222, Jul 1967.

[43] J. H. Malmberg, C. B. Wharton, R. W. Gould, and T. M. O'Neil, "Plasma wave echo experiment," *Phys. Rev. Lett.*, vol. 20, pp. 95–97, Jan 1968.

[44] E. Ott, "Relativistic synchrotron plasma echo," *Journal of Plasma Physics*, vol. 4, pp. 471–476, Sept. 1970.

[45] G. Morigi, E. Solano, B.-G. Englert, and H. Walther, "Measuring irreversible dynamics of a quantum harmonic oscillator," *Phys. Rev. A*, vol. 65, p. 040102, Apr 2002.

[46] T. Meunier, S. Gleyzes, P. Maioli, A. Auffeves, G. Nogues, M. Brune, J. M. Raimond, and S. Haroche, "Rabi oscillations revival induced by time reversal: A test of mesoscopic quantum coherence," *Phys. Rev. Lett.*, vol. 94, p. 010401, Jan 2005.

[47] A. Bulatov, A. Kuklov, B. E. Vugmeister, and H. Rabitz, "Echo in optical lattices: Stimulated revival of breathing oscillations," *Phys. Rev. A*, vol. 57, pp. 3788–3792, May 1998.

[48] N. Piovella, V. Beretta, G. R. M. Robb, and R. Bonifacio, "Photon echo in the super-radiant light scattering from a Bose-Einstein condensate," *Phys. Rev. A*, vol. 68, p. 021801, Aug 2003.

[49] F. B. J. Buchkremer, R. Dumke, H. Levsen, G. Birkl, and W. Ertmer, "Wave packet echoes in the motion of trapped atoms," *Phys. Rev. Lett.*, vol. 85, pp. 3121–3124, Oct 2000.

[50] S. Maneshi, J. F. Kanem, C. Zhuang, M. Partlow, and A. M. Steinberg, "Efficient vibrational state coupling in an optical tilted-washboard potential via multiple spatial translations and application to pulse echoes," *Phys. Rev. A*, vol. 77, p. 022303, Feb 2008.

[51] M. F. Andersen, A. Kaplan, and N. Davidson, "Echo spectroscopy and quantum stability of trapped atoms," *Phys. Rev. Lett.*, vol. 90, p. 023001, Jan 2003.

[52] S. Elyutin, "Echo responses of an ensemble of cold atoms in optical lattices," *Optics and Spectroscopy*, vol. 98, pp. 605–617, Apr 2005. 10.1134/1.1914901.

[53] G. Raithel, W. D. Phillips, and S. L. Rolston, "Collapse and revivals of wave packets in optical lattices," *Phys. Rev. Lett.*, vol. 81, pp. 3615–3618, Oct 1998.

[54] L. Pitaevskii, "Phenomenological theory of mode collapse-revival in a confined Bose gas," *Physics Letters A*, vol. 229, pp. 406–410, Jun 1997.

[55] R. Robinett, "Quantum wave packet revivals," *Physics Reports*, vol. 392, pp. 1–119, Mar 2004.

[56] J. H. Eberly, N. B. Narozhny, and J. J. Sanchez-Mondragon, "Periodic spontaneous collapse and revival in a simple quantum model," *Phys. Rev. Lett.*, vol. 44, pp. 1323–1326, May 1980.

[57] V. Bužek and P. Knight, *I: Quantum Interference, Superposition States of Light, and Nonclassical Effects*, vol. 34, pp. 1–158. Elsevier, 1995.

[58] D. M. Meekhof, C. Monroe, B. E. King, W. M. Itano, and D. J. Wineland, "Generation of nonclassical motional states of a trapped atom," *Phys. Rev. Lett.*, vol. 76, pp. 1796–1799, Mar 1996.

[59] M. Brune, F. Schmidt-Kaler, A. Maali, J. Dreyer, E. Hagley, J. M. Raimond, and S. Haroche, "Quantum rabi oscillation: A direct test of field quantization in a cavity," *Phys. Rev. Lett.*, vol. 76, pp. 1800–1803, Mar 1996.

[60] M. Hofheinz, E. M. Weig, M. Ansmann, R. C. Bialczak, E. Lucero, M. Neeley, A. D. O'Connell, H. Wang, J. M. Martinis, and A. N. Cleland, "Generation of fock states in a superconducting quantum circuit," *Nature*, vol. 454, pp. 310–314, July 2008.

[61] J. J. Sakurai, *Modern Quantum Mechanics*. Reading, MA: Addison-Wesley Publishing Company, Revised ed., 1994.

[62] P. Kasperkovitz and M. Peev, "Long-time evolution of semiclassical states in anharmonic potentials," *Phys. Rev. Lett.*, vol. 75, pp. 990–993, Aug 1995.

[63] G. Manfredi and M. R. Feix, "Theory and simulation of classical and quantum echoes," *Phys. Rev. E*, vol. 53, pp. 6460–6470, Jun 1996.

[64] E. Gross, "Structure of a quantized vortex in boson systems," *Il Nuovo Cimento (1955-1965)*, vol. 20, pp. 454–477, May 1961. 10.1007/BF02731494.

[65] L. P. Pitaevskii, "Vortex lines in an imperfect Bose gas," *Soviet Phys.* JETP, vol. 13, pp. 451–454, 1961.

[66] S. Stringari, "Collective excitations of a trapped Bose-condensed gas," *Phys. Rev. Lett.*, vol. 77, pp. 2360–2363, Sep 1996.

[67] M.-O. Mewes, M. R. Andrews, N. J. van Druten, D. M. Kurn, D. S. Durfee, C. G. Townsend, and W. Ketterle, "Collective excitations of a Bose-Einstein condensate in a magnetic trap," *Phys. Rev. Lett.*, vol. 77, pp. 988–991, Aug 1996.

[68] B. Chakrabarti, T. K. Das, and P. K. Debnath, "Stability of a Bose-Einstein condensate in an anharmonic trap," *Phys. Rev. A*, vol. 79, p. 053629, May 2009.

[69] D. A. Zezyulin, G. L. Alfimov, V. V. Konotop, and V. M. Pérez-García, "Stability of excited states of a Bose-Einstein condensate in an anharmonic trap," *Phys. Rev. A*, vol. 78, p. 013606, Jul 2008.

[70] P. K. Debnath and B. Chakrabarti, "Instability of collective excitations and power laws of an attractive Bose-Einstein condensate in an anharmonic trap," *Phys. Rev. A*, vol. 82, p. 043614, Oct 2010.

[71] G.-Q. Li, L.-B. Fu, J.-K. Xue, X.-Z. Chen, and J. Liu, "Collective excitations of a Bose-Einstein condensate in an anharmonic trap," *Phys. Rev. A*, vol. 74, p. 055601, Nov 2006.

[72] H. Ott, J. Fortágh, and C. Zimmermann, "Dynamics of a Bose–Einstein condensate in an anharmonic trap," *Journal of Physics B: Atomic, Molecular and Optical Physics*, vol. 36, p. 2817, June 2003.

[73] D. S. Jin, J. R. Ensher, M. R. Matthews, C. E. Wieman, and E. A. Cornell, "Collective excitations of a Bose-Einstein condensate in a dilute gas," *Phys. Rev. Lett.*, vol. 77, pp. 420–423, Jul 1996.

[74] H. Ott, J. Fortágh, S. Kraft, A. Günther, D. Komma, and C. Zimmermann, "Nonlinear dynamics of a Bose-Einstein condensate in a magnetic waveguide," *Phys. Rev. Lett.*, vol. 91, p. 040402, Jul 2003.

[75] V. Bretin, S. Stock, Y. Seurin, and J. Dalibard, "Fast rotation of a Bose-Einstein condensate," *Phys. Rev. Lett.*, vol. 92, p. 050403, Feb 2004.

[76] K. Strecker, G. Partridge, A. Truscott, and R. Hulet, "Formation and propagation of matter-wave soliton trains," *Nature*, vol. 417, pp. 150–153, May 2002.

[77] S. L. Cornish, S. T. Thompson, and C. E. Wieman, "Formation of bright matter-wave solitons during the collapse of attractive Bose-Einstein condensates," *Phys. Rev. Lett.*, vol. 96, p. 170401, May 2006.

[78] B. Deissler, M. Zaccanti, G. Roati, C. D'Errico, M. Fattori, M. Modugno, G. Modugno, and M. Inguscio, "Delocalization of a disordered bosonic system by repulsive interactions," *Nature Physics*, vol. 6, pp. 354–358, Apr 2010.

[79] M. Fattori, C. D'Errico, G. Roati, M. Zaccanti, M. Jona-Lasinio, M. Modugno, M. Inguscio, and G. Modugno, "Atom interferometry with a weakly interacting Bose-Einstein condensate," *Phys. Rev. Lett.*, vol. 100, p. 080405, Feb 2008.

[80] A. Buchleitner, D. Delande, and J. Zakrzewski, "Non-dispersive wave packets in periodically driven quantum systems," *Physics Reports*, vol. 368, pp. 409–547, Oct 2002.

[81] E. A. Shapiro, I. A. Walmsley, and M. Y. Ivanov, "Suppression of decoherence in a wave packet via nonlinear resonance," *Phys. Rev. Lett.*, vol. 98, p. 050501, Jan 2007.

[82] J. Henkel and M. Holthaus, "Classical resonances in quantum mechanics," *Phys. Rev. A*, vol. 45, pp. 1978–1986, Feb 1992.

[83] H. Maeda and T. F. Gallagher, "Nondispersing wave packets," *Phys. Rev. A*, vol. 75, p. 033410, Mar 2007.

[84] R. Fedele, "From maxwell's theory of saturn's rings to the negative mass instability," *Phil. Trans. R. Soc. A*, vol. 366, pp. 1717–1733, May 2008.

[85] C. D. Fertig, K. M. O'Hara, J. H. Huckans, S. L. Rolston, W. D. Phillips, and J. V. Porto, "Strongly inhibited transport of a degenerate 1d Bose gas in a lattice," *Phys. Rev. Lett.*, vol. 94, p. 120403, Apr 2005.

[86] E. Wigner, "On the quantum correction for thermodynamic equilibrium," *Phys. Rev.*, vol. 40, pp. 749–759, Jun 1932.

[87] M. Hillery, R. O'connell, M. Scully, and E. P. Wigner, "Distribution functions in physics: fundamentals," *Physics Reports*, vol. 106, pp. 121–167, Apr 1984.

[88] K. Husimi, "Some formal properties of the density matrix," in *Proc. Phys.-Math. Soc. Japan*, vol. 22, pp. 264–314, 1940.

[89] J. E. Harriman, "Some properties of the Husimi function," *The Journal of Chemical Physics*, vol. 88, p. 6399, May 1988.

[90] G. P. Agrawal, *Nonlinear Fiber Optics*. Academic Press, Inc., 1995.

[91] J. Javanainen and J. Ruostekoski, "Symbolic calculation in development of algorithms: split-step methods for the Gross-Pitaevskii equation," *Journal of Physics. A, Mathematical and General*, vol. 39, Mar 2006.